國立交通大學

應用化學研究所

碩 士 論 文

磁性奈米碳管之製備以及與A549和HeLa細胞之交互作用

Fabrication of Magnetic CNTs and Interaction with A549 and HeLa Cancer Cells

研 究 生：郭奕廷

指導教授：裘性天　教授

陳月枝　教授

中 華 民 國 九 十 九 年 六 月

磁性奈米碳管之製備以及與 A549 和 HeLa 細胞之交互作用

Fabrication of Magnetic CNTs and Interaction with A549 and HeLa Cancer Cells

研 究 生：郭奕廷　　Student：Yi-Ting Kuo

指導教授：裘性天　　Advisor：Hsin-Tien Chiu

Yu-Chie Chen

國 立 交 通 大 學

應 用 化 學 研 究 所

碩 士 論 文

A Thesis

Submitted to Institute of Applied Chemistry

College of Science

National Chiao Tung University

In partial Fulfillment of the Requirements

for the Degree of Master of Science

in

Applied Chemistry

June 2010

Hsinchu, Taiwan, Republic of China

中華民國九十九年六月

Contents

Fabrication of Magnetic CNTs and Interaction with A549 and HeLa Cancer Cells

Student: Yi-Ting Kuo

Advisor: Dr. Hsin-Tien Chiu
Dr. Yu-Chie Chen

Abstract

Carbon nanotubes (CNTs) have strong absorbances in near-infrared (NIR) region, a great biocompatibility and the surface can be modified easily by biomolecular. These unique properties make CNTs promising candidates for multifunctional biological transporters and thermal cancer cell killers. Incorporating Fe_3O_4 nanoparticles into the CNTs can enhance effective CNT separation by magnetism. Therefore, here we report the synthesis of magnetic carbon nanotubes (MCNTs) by using chemical vapor deposition (CVD) and chemical coprecipitation for biomedical applications. We investigated the cytotoxic effects of MCNTs using A549 and HeLa cancer cells with MTT [(3-(4,5-Dimethylthiazol-2-yl)-2, 5-diphenyltetrazolium bromide] assay. We found that MCNTs, below 2 μg/μL, have a very good biocompatibility for A549 cells. Furthermore, this work demonstrates that continuous 808 nm NIR radiations triggered extensive cell death in the presence of MCNTs because of the excessive local heating *in vitro*. In addition, we also studied cellular uptake of MCNTs mechanism. It was found that the cellular uptake was much higher in cells exposed to MCNT in an FA-free culture medium than those in a culture medium with FA after incubation 16 h. We found that incubation with endocytosis inhibitor agent did not influence cellular uptake of MCNTs. It is clear that the uptake mechanism is likely to be an endocytosis-independent pathway.

磁性奈米碳管之製備以及與 A549 和 HeLa 細胞之交互作用

研究生：郭奕廷　　指導教授： 裘性天 博士

陳月枝 博士

摘要

奈米碳管能夠吸收近紅外光將其轉換成熱能以及具有良好的生物相容性和表面易修飾生物分子之特性，由於這些獨特的特性使得奈米碳管成為多功能性生物載體及熱殺死癌細胞的最佳選擇。若能將氧化鐵奈米粒子填入到奈米碳管中，就可以藉由磁性有效的分離出碳管。因此，在這裡我們利用化學氣相沉積法和化學共沉澱法合成出磁性奈米碳管做為生醫應用的材料。我們利用 MTT 分析法研究磁性奈米碳管對 A549 和 HeLa 細胞是否具有毒性。當磁性奈米碳管的濃度低於 2 μg/μL 時，其對 A549 細胞具有一個良好的生物相容性。此外，這個研究也證實了在試管內的磁性奈米碳管被波長 808 nm 的近紅外光連續照射會引起局部的加熱導致大量的細胞死亡。另外，我們也研究癌細胞攝取磁性奈米碳管的機制。癌細胞培養 16 小時之後，我們發現在沒有葉酸的培養液中癌細胞攝取磁性奈米碳管的數量多於含有葉酸的培養液並且將癌細胞與胞吞抑制劑一起培養，發現並不會影響癌細胞攝取磁性奈米碳管。因此，癌細胞攝取的機制或許不依賴胞吞作用。

Acknowledgments

首先，我要感謝裘老大在兩年前收留了懵懵懂懂的我，真的很感謝裘老大這兩年來的指導以及鼓勵，在實驗上給予我很大的空間發展，並在我氣餒的時後適時的指引我光明的道路，讓我可以克服困難。日常生活的相處，裘老大的裘式幽默總是能帶給大家歡笑，使得裘性天實驗室這個大家族能夠這麼的團結氣氛良好。在這不長不短的歲月裡，能夠在這麼優良的實驗室裡做實驗，我感到很開心，在此謹致最深的謝意，謝謝裘老師。同時也要感謝李紫原教授，這兩年來在 meeting 上給予我無數的指導，讓我對於學術上的認知有更進一步成長。此外，也要感謝陳月枝教授提供實驗室的器材設備以及所提出的各項建議，使學生的論文能夠順利完成並且更加完善，謝謝每一位老師的用心指導以及鼓勵，學生會謹記在心。

感謝裘性天實驗室裡的每一位夥伴，還有讓我又愛又恨的學長兼老師-張裕煦，如果沒有張老師的諄諄教誨，培養出我對實驗的嚴謹態度，或許沒有現在的我。此外，Baken 學姊每次在我抱怨的時候總是會給我鼓勵和打氣，彭治偉和黃亭凱學長總是打球的好夥伴，會適時補刀的美麗俏佳人佳兒學姐，在我最急迫的時候給予我很大的幫助，真的非常感謝。蕭蕭爽朗的笑聲總是很有穿透力，結婚快樂唷，要甜甜蜜蜜的走下去，別在化學年會前一天借不到車子了！總是掛著笑容

的 WeiWei 謝謝你的打薄剪還有工作要順順利利的唷！排球高手大銘，祝福你考試順利，把 WeiWei 娶回家也順利唷，呵呵。傻呼呼的亦諄總是麻煩你去幫我借細胞，真的很感謝你。搞笑又很宅的昱良，不要再待在家打魔獸和看大聯盟了，快點交女朋友吧！也謝謝你總是和我一起討論實驗的問題以及當我的垃圾桶。小親親凱捷，等我當兵閒閒的時候再來個無數場，看我怎麼殺到你變苦瓜臉，洗好勃子等著我呀！也祝福你博士生涯順利和昱良一起交到女朋友 XD。總是學昱良學的很像的佑蕙以及愛吃美食且有良好運動細胞的心安，希望你們都能夠找到理想的工作唷！每次都要一腳爆射的 kimi，還記得我們一起踢進系際盃嗎?很高興能夠和你一起踢球，有機會要再一起踢唷！也祝福你當兵順利囉，我看到你可以不要說楊排長好嗎 XD。帥氣的小童，對於任何事情你真的都是以很認真負責的態度去對待，希望你在實驗上也能夠有好的進展。是北科也是交大的學弟鄒宗育，雖然和你說話的次數不多，但是我知道其實你心地很善良，謝謝你幫忙我處理口試採買的事情。還有小栗、大叔、采蓉、巴斯、張大哥、韓三、Lisa、旻橋、婷婷、久萱、柏欽、奕仁等，很感謝你們在實驗上的幫助、建議和鼓勵。真的很開心能夠和你們大家相識並在同一個實驗室裡，讓我的研究生活可以這麼的有趣。最後要感謝我的父母與姐姐，這些年來默默的支持給予我鼓勵，讓我可以順利的完成學業，謝謝你們。

List of Tables

List of Figures

Chapter 1 Introduction

1.1 Template assisted synthesis

Many methods can fabricate nanomaterials, one of them is called template assisted synthesis. Nanostructured templates of polycarbonate, anodic aluminum oxide (AAO) membranes, glass membranes and mesoporous zeolites etc. have been fabricated. [1] These templates have different geometries. They can be fabricated into one dimensional (1D), two dimensional (2D) and three dimensional (3D) nanostructures. Fabrication of 1D and 2D nanostructures usually use polycarbonate and AAO templates. Polycarbonate templates from chemical etching manner result in porous structure randomly distributed over the surface of the membrane. On the other hand, AAO membranes are used frequently to aid the formation of wires,[2] tubes[3] and rods[4] inside their channels. AAO templates provide uniform nanoscale pore size distribution. Further pore size and distribution density can be controlled by adjusting fabrication temperature, electrolyte and voltage. The templates have large scale pore-array to aid the filling of carbon,[3,5] metal,[2,6] semiconductor[6,7] and polymer[1,6] substance by using chemical vapor deposition (CVD),[5] electro-deposition process to synthesize 1D materials.[1] Herein, we use AAO as the template and CVD process to synthesize carbon nanotubes (CNTs) by pyrolyzing acetylene inside the AAO channels.

1.2 New forms of carbon

Before 1980, carbon was known to exist in three allotropes forms only: amorphous, graphite and diamond.[8] However, carbon is found in four forms now: amorphous, graphite, diamond and fullerene. The newly discovered fullerenes are classified into two forms: the sphere shaped molecules are called fullerenes or bucky balls (Figure 1.1) and the tube shaped molecules called carbon nanotubes. In 1985, Kroto and Smally et al. found fullerene by mass spectrometry.[9] In 1990, W. Kratschmer obtained a large of amount fullerenes on graphite electrode by direct

current arc discharge method.[10] This new form of carbon interests scientists. After the discovery of fullerene, S. Iijima also found carbon nanotubes.[11] The drawback of the synthesis was that the yield was too low. Therefore, a large scale synthesis, controlling the growth-orientation and improving the purity are important.

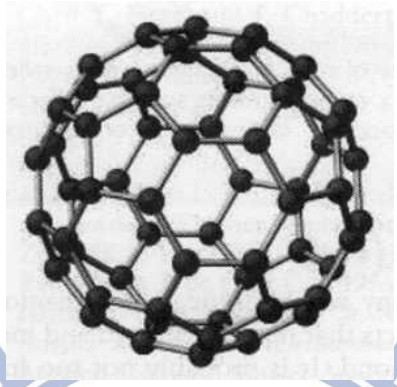

Figure 1.1 Fullerene C_{60} or bucky ball. [8]

1.3 Carbon nanotube

1.3.1 Type of nanotubes

Single-walled nanotubes (SWNTs) have many different tubular structure because of graphitic sheets can be rolled in different directions. The normal method express the rolling process is determined by vector : $R = na_1 + ma_2$, where n and m are integers (Figure 1.2). When $na_1 = 0$ or $ma_2 = 0$, one vector na_1 defines a horizontal line on the graphite sheet and forms a zigzag nanotube. When $na_1 = ma_2$, then a line pass across each hexagon, dividing them into two equal parts, and forms an armchair nanotube. For the third type, na_1 and ma_2 are not zero and not equal. These form a chiral nanotube (Figure 1.3). A nanotube can have one layer, two layers and many layers of graphenes. These are called single-walled nanotube (SWNT), double-walled nanotube (DWNT), multi-walled nanotube (MWNT), respectively. Depending on the synthesis and post-processing methods, CNTs with different physical characteristics can be produced. They can be metallic, semiconducting and nonmetallic.

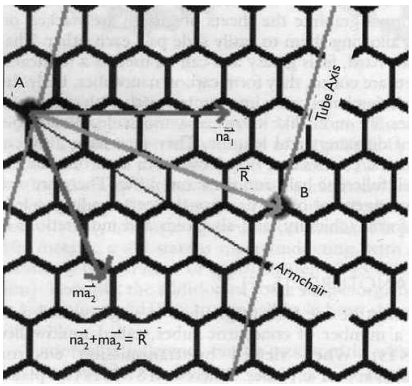

Figure 1.2 Naming nanotubes. [8]

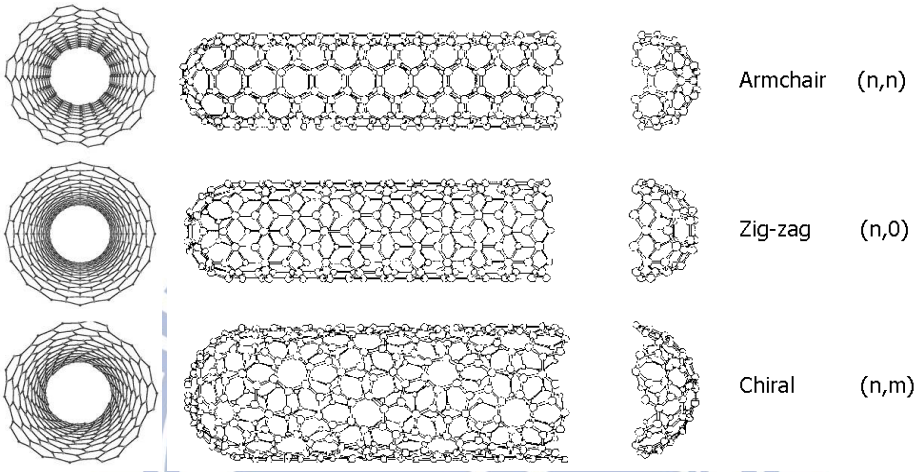

Figure 1.3 Different types of SWNTs.[8]

1.3.2 Carbon nanotube synthesis

Carbon nanotubes are one of the most important materials in nanotechnology. It is widely investigated because of their unique electrical, chemical, thermal and mechanical properties. These are due to the specific arrangement of the carbon atoms. It can be applied in composite materials, biomedical applications and electronics to energy storage. Numerous methods to grow CNT have been developed, for example:

1. Arc-discharge: First method for producing C_{60} fullerenes, is the most common and perhaps easiest method to fabricate CNTs. This method creates CNTs through arc-vaporization of two carbon electrodes (anode and cathode) when they are close together. They are separated by approximately 1 mm, in a close system filled with inert gas (Ar or He gas) at low pressure (Figure 1.4). A direct current of 50 to 100 A, driven by a potential difference of approximately 20 V, creates a

high temperature (close to 3500 ^{o}C) discharge between the two electrodes. The discharge vaporizes the surface of anode carbon electrodes. This forms a rod-like deposit on the cathode electrode, with C_{60} fullerenes and CNTs mixed in the soot formed. However, this technique produces a complex mixture of components. Further purification is required to separate the CNTs from the soot and the residual catalytic metals in the crude product. [8, 12]

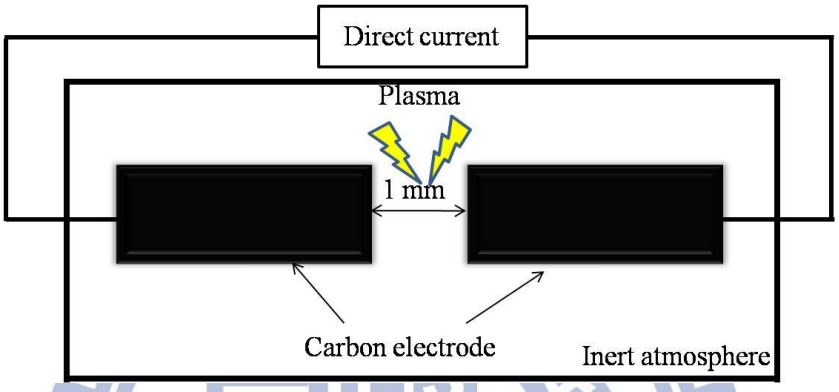

Figure 1.4 Experimental setup for arc discharge method.[12]

2. Laser ablation: In 1996 CNTs were first synthesized using a dual-pulsed laser. High quality SWNT (> 70 wt% purity) in gram quantities can be obtained. In this process, CNTs were prepared by laser vaporization of the carbon target containing 50:50 mixture of Ni and Co powder in a flowing inert gas tube furnace heated to 1200 ^{o}C, followed by heat treatment in vacuum at 1000 ^{o}C to remove the fullerenes (Figure 1.5). The use of two successive laser pulses vaporizes the target more uniformly and minimizes the amount of carbon deposited as soot. The second laser pulses disintegrate large particles ablated by the first laser, allowing them growing into the nanotube structures. The as-produced SWNTs are usually in the form of ropes consisting of ten of 10 - 20 nm in diameter and up to 100 μm or more in length for individual CNTs. By varying the growth parameters for example, temperature and catalyst composition, the nanotube diameter and distribution can be varied. [8, 12]

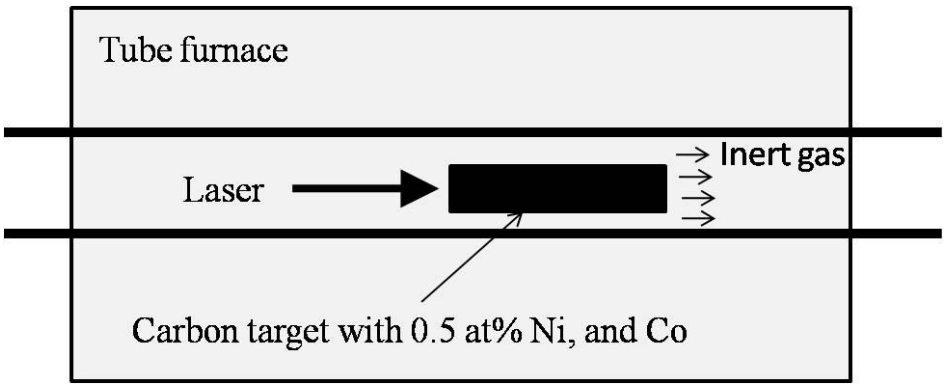

Figure 1.5 Experimental setup for laser ablation method.[12]

3. Chemical vapor deposition: This process have many methods, for example, thermal CVD, plasma enhanced CVD and low pressure CVD etc. The CNTs growth of CNTs by CVD involves catalytic decomposition of hydrocarbon gases (acetylene, C_2H_2; ethylene, C_2H_4; xylene, C_8H_{10} or benzene, C_6H_6) on catalytic nanoparticles, such as Fe, Co and Ni at high temperature (500 to 800 ^oC). By CVD methods, CNTs may be easily aligned with others and grow perpendicular to the substrate. [8, 12]

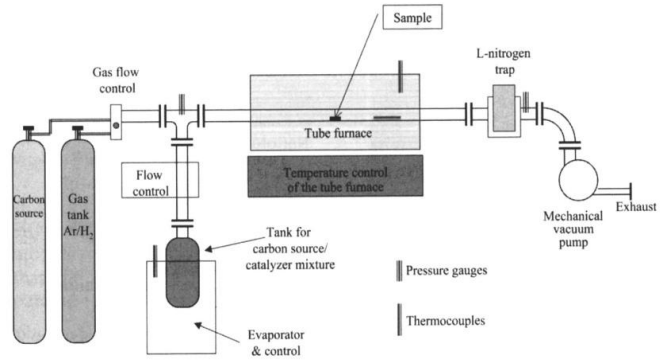

Figure 1.6 Experimental setup for CVD method.[12]

Although arc discharge and laser ablation methods are currently the primary methods for fabrication quantities of high quality carbon nanotubes but both methods have some drawback. First, both methods are costly because of the high temperature processes and the limited number of CNTs produced. Second, both methods grow CNTs in highly entangled forms with unwanted carbon and metal impurities. Also, using above methods is impossible to control selective growths

at specific locations. Thus, it is difficult to build highly organized CNT structures. On the other hand, CVD methods may overcome these and become a powerful candidate for large scale fabrication of CNTs. Consequently, we choose a CVD method complied with AAO templates to synthesize our CNTs. Comparison of three methods is shown in Table 1.1.

In addition to methods discussed above, other methods such as ball milling, diffusion flame synthesis, solar energy, heat treatment of a polymer, electrolysis and low temperature solid pyrolysis can also produce CNTs.[8]

Table 1.1 Comparison of CNT syntheses

Synthesis method	Principle	Advantage	Disadvantage
Arc discharge	Passing direct current through graphite rod to produce arc in inert atmosphere. Pressure: 200~500 torr Current: 50~100 A Potential: 19~25 V	1. Produce MWNT/SWNT 2. Process is simple	1. Low yield 2. Costly 3. Product needs purification
Laser ablation	Using laser pulse to hit carbon target containing metal catalysts.	1. Produce SWNT 2. High degree of graphitization	1. Low yield 2. Costly 3. CNT contains metal catalyst particles
Chemical vapor deposition	Catalytic decomposition of hydrocarbon gases on catalytic nanoparticles at high temperature (500 to 800 ^{o}C).	1. Equipment is simple 2. Low temperature 3. High yield 4. CNTs aligned easily 5. Reaction process is easy controlled easily	1. Low degree of graphitization 2. CNTs surface have amorphous carbon and small amount of defect 3. CNT may contain metal catalyst particles

1.4 Magnetic materials

Magnetic nanoparticles have been extensively exploited in our lives, for instance, electrochemical capacitors, storage information, biosensor and other biomedical applications.[21-26] Ferromagnetic material is usually applied in all of magnetic materials. Magnetic materials size is gradually decrease with nanotechnology advancement and can produce unique properties with the size decrease to nanograde. In electromechanical engineering, the device volume become light, thin, low-energy, and sensitivity when magnetic materials size is small. Storage medium density is increased with decreasing magnetic nanoparticle size.[27] Magnetic nanoparticles also have many biomedical applications including imaging, separation, drug delivery, and cancer therapy. For example, magnetic nanoparticles can improve magnetic resonance imaging (MRI) resolution and increase MRI contrast which can enhance the observation of organism structure (Figure 1.7).[28] When CNTs and magnetic nanoparticles integrate into MCNTs, the applications will be widened. For example, the blood cells attached with MCNTs can be manipulated in a magnetic field.[29] In literature, CVD,[30-32] ectrodeposition,[33] and ferrofluids-filling[34] methods are usually used to synthesize MCNTs. Yield and properties of the magnetic substance are different in various MCNT synthesis processes.

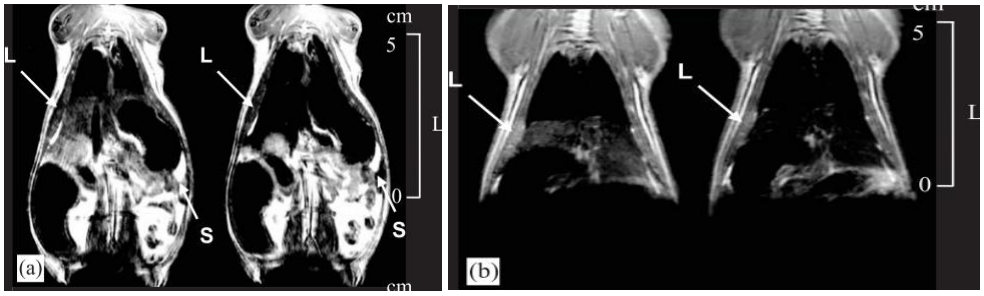

Figure 1.7 (a), (b) MR images of rats collected pre (left) and 30 min post (right) injection of Fe colloidal dispersion. L is liver and S is spleen.[28]

1.5 Magnetic properties

Substance is composed of nucleus, which contains protons and neutrons, electrons. An atom has magnetic moments that originate from nucleus spins and electron spins. Magnetic moments from nucleus can be ignored because it is substantially less than the magnetic moments producing electrons. Every substance has different magnetize property. This section provides a brief description of five magnetisms.

1.5.1 Diamagnetism

Diamagnetism is a very weak form of magnetism and the volume susceptibility (χ) for diamagnetic solid materials is on the order of -10^{-5} (Table 1.2). When a diamagnetic material is placed in a magnetic field, the induced magnetization in the material is in a direction opposite to that of the applied magnetizing field. Thus, χ is negative and it can be interpreted as the substance trying to expel the applied field out from the material. Atoms of a diamagnetic material show no net magnetic moment in the absence of an applied magnetic field. In the presence of an applied magnetic field, a net magnetic moment is induced. It is aligned opposite to the field direction (Figure 1.8). Diamagnetism is found in all materials, but because it is so weak, it can be observed only when other types of magnetism are totally absent.

Figure 1.8 The atomic dipole configuration for a diamagnetic material with and without a magnetic field.[35]

1.5.2 Paramagnetism

Susceptibilities for paramagnetic materials have values varying from 10^{-5} to 10^{-2} (Table 1.2). In the absence of an external magnetic field, the orientation of these magnetic moments are random. The result is that a piece of the material possesses no net macroscopic magnetization. These atomic magnetic moments are free to rotate. Without an external field, these magnetic dipoles are acted individually with no mutual interaction between adjacent dipoles as shown in Figure 1.9. In the presence of an applied magnetic field, the dipoles align somewhat along the field, thus, χ is positive (Figure 1.9).

Figure 1.9 Atomic dipole configuration with and without an external magnetic field for a paramagnetic material.[35]

Table 1.2 Room-temperature magnetic susceptibilities for diamagnetic and paramagnetic materials.[35]

Diamagnetics		*Paramagnetics*	
Material	*Susceptibility χ_m (volume) (SI units)*	*Material*	*Susceptibility χ_m (volume) (SI units)*
Aluminum oxide	-1.81×10^{-5}	Aluminum	2.07×10^{-5}
Copper	-0.96×10^{-5}	Chromium	3.13×10^{-4}
Gold	-3.44×10^{-5}	Chromium chloride	1.51×10^{-3}
Mercury	-2.85×10^{-5}	Manganese sulfate	3.70×10^{-3}
Silicon	-0.41×10^{-5}	Molybdenum	1.19×10^{-4}
Silver	-2.38×10^{-5}	Sodium	8.48×10^{-6}
Sodium chloride	-1.41×10^{-5}	Titanium	1.81×10^{-4}
Zinc	-1.56×10^{-5}	Zirconium	1.09×10^{-4}

1.5.3 Ferromagnetism

Certain metallic materials possess a large magnetic moment even in the absence of an external magnetic field. The succeptibility χ is very large ~ 10^6 (even infinite) and further depends on the applied field intensity. Every piece of ferromagnetic material should have a strong magnetic field, but ferromagnets are often found in an "unmagnetized" state. The reason for this is that a bulk piece of ferromagnetic material is divided into many tiny magnetic domains. Within each domain, the spins are aligned, but (if the bulk material is in its lowest energy configuration, i.e. "unmagnetized"), the spins of separate domains point in different directions and their magnetic fields cancel out, so the object has no net large scale magnetic field (Figure 1.10a). Ferromagnetic materials tend to divide into magnetic domains because this is a lower energy configuration. Thus, an ordinary piece of iron generally has little or no net magnetic moment. However, if it is placed in a strong external magnetic field, the domains will re-orient in parallel with that field, and will remain oriented when the field is turned off, thus creating a "permanent" magnet. The domains do not go back to their original minimum energy configuration when the field is turned off because the domain walls tend to become 'pinned' or 'snagged' on defects in the crystal lattice, preserving their parallel orientation (Figure 1.10b).[35,36]

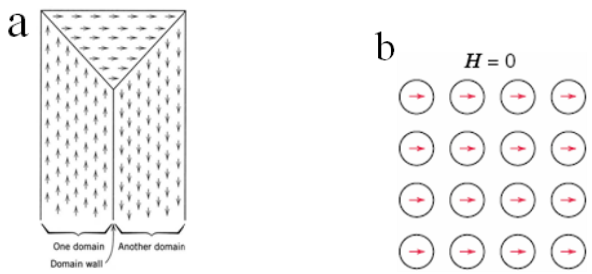

Figure 1.10 (a) Domain in a ferromagnetic material, arrows represent atomic magnetic dipoles. (b) The mutual alignment of atomic dipoles for a ferromagnetic material, which will exist even in the absence of an external magnetic field.[35]

1.5.4 Antiferromagnetism

In one such group, spin coupling results in an antiparallel alignment i.e. alignment of spin moments of adjacent atom or ions in opposite directions is termed as antiferromagnetism. Antiferromagnetic materials with atoms at alternate positions have their spins aligned in opposite directions. This results in complete cancellation of the magnetic moments and net zero magnetization. Manganese oxide (MnO) exhibits antiferromagnetic behavior as shown in Figure 1.11. No net magnetic moment is associated with the O^{2-} ions. The magnetic moment of Mn^{2+} ions at corners of a cubic unit cell are aligned in one directions while those at face centers are in opposite directions thereby leading to complete cancellation of the magnetic moments and resulting in net zero magnetic moment.

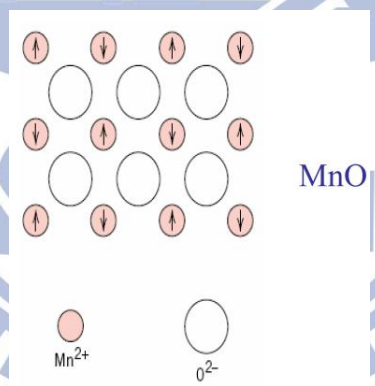

Figure 1.11 Schematic representation of antiparallel alignment of spin magnetic moments for antiferromagnetic manganese oxide.[35]

1.5.5 Ferrimagnetism

The phenomenon of ferrimagnetism is similar to antiferromagnetism but there is no complete cancellation of spin of adjacent atoms because of different type of atoms/ions occupying these positions and a spontaneous magnetization remains. The macroscopic magnetic characteristics of ferromagnets and ferrimagnets materials are similar. The difference is in the magnitude of magnetic moments. The prototype

ferrite is Fe_3O_4. Fe_3O_4 is basically $FeOFe_2O_3$ $[Fe^{2+}O^{2-}(Fe^{3+})_2(O^{2-})_3]$ in which Fe ions exists in both +2 and +3 valence states in the ratio of 1:2 (Figure 1.12). According to Table 1.3, we know that net magnetic moments are not zero.

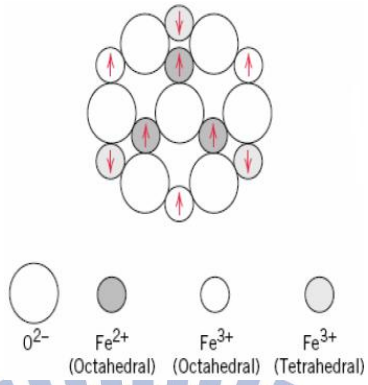

Figure 1.12 The spin magnetic moment configuration for Fe^{2+} and Fe^{3+} iron in Fe_3O_4.[35]

Table 1.3 The distribution of spin magnetic moments for Fe^{2+} and Fe^{3+} ions in a unit cell of Fe_3O_4.[35]

Cation	*Octahedral Lattice Site*	*Tetrahedral Lattice Site*	*Net Magnetic Moment*
Fe^{3+}	↑↑↑↑ ↑↑↑↑	↓↓↓↓ ↓↓↓↓	Complete cancellation
Fe^{2+}	↑↑↑↑ ↑↑↑↑	—	↑↑↑↑ ↑↑↑↑

[a] Each arrow represents the magnetic moment orientation for one of the cations.

1.5.6 Superparamagnetism

Superparamagnetism is similar to paramagnetism. In small enough nanoparticles, magnetization can randomly flip direction under the influence of temperature (Figure 1.13). When the nanoparticle size decreases towards critical particle diameter ($D_{critical}$), the coercivity increases toward maximum value and the multi-domain structure changes into the single domain one. When the nanoparticle size continues to decrease below the single domain value, the coercivity decreases to zero and the system becomes superparamagnetic with no hysteresis (Figure 1.14). Different magnetic nanoparticles have various critical sizes shown in Figure 1.15.

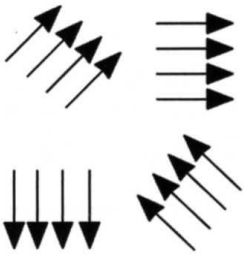

Figure 1.13 Schematic representation of spin magnetic moments for superparamagnetism.[37]

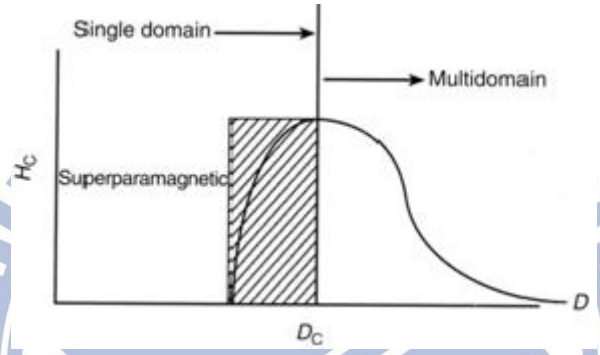

Figure 1.14 Qualitative illustration of the behavior of the coercivity in ultrafine particle system as the particle size changes.[37]

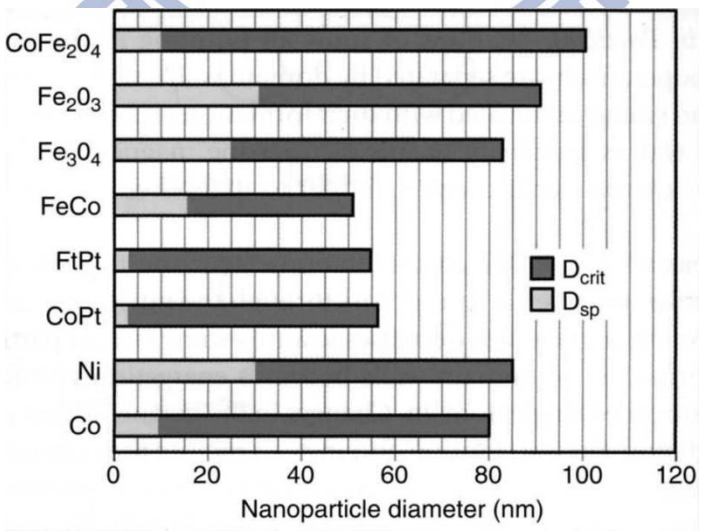

Figure 1.15 Single domain size, D_{crit} and magnetic stability size or the superparamanetic limit at room temperature, D_{sp} for some common ferromagnetic materials.[37]

1.5.7 Hysteresis curve

A hysteresis loop shows the relationship between the induced magnetic flux density (B) and the magnetizing force (H). It is often referred to as the B-H loop. An example hysteresis loop is shown in Figure 1.16.

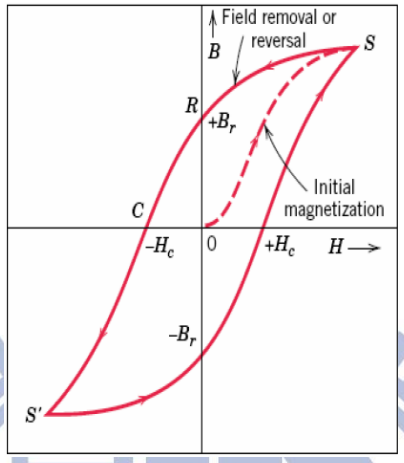

Figure 1.16 Hysteresis loop of ferromagnetic material.[35]

A ferromagnetic material is initially unmagnetized then it will follow the dashed line as H is increased. At point "S" almost all of the magnetic domains are aligned and the material has reached the point of magnetic saturation. When H is reduced to zero, the curve will move from point "S" to point "R". At this point, there exists a residual B field that is called the remanence, or remanent flux density, B_r, the material remains magnetized in the absence of an external H field. As the magnetizing force is reversed, the curve moves to point "C", where the flux has been reduced to zero. This is called the point of coercivity on the curve. The force required to remove the residual magnetism from the material is called the coercive force or coercivity of the material (H_c). As the magnetizing force is increased in the negative direction, the material will again become magnetically saturated but in the opposite direction (point "S'"). A second reversal of the field to the point of the initial saturation (point S) completes the symmetrical hysteresis loop and also yields both a negative romance ($-B_r$) and a positive coercivity ($+H_c$).

1.6 Folic acid

The term folic acid (also known as vitamin B_9) is used to denote pteroylmonoglutamic acid. The folic acid (FA) is divided into three parts (Figure 1.17): pteridine (left), para amino benzoic acid (middle), glutamic acid (right). Glutamic acid has α- and γ-carboxylic acids, but γ-carboxylic acid is more selectively activated due to its higher reactivity.[38] Folic acid is not stable in acid solution. It is very stable in pH 5~7 and sensitive to light. Folic acid is an important factor for cell growth and division. It is necessary for the production and maintenance of new cells, for DNA synthesis and RNA synthesis. Tumor needs more nutrients in division so that many cancer cells' surface has overexpressed folate receptors (FRs). Thus, folate has high specific affinity to cancer cells. According to the above reasons, cancer cells can capture material–modified by FA. This method is called receptor-mediated endocytosis (Figure 1.18). It can be applied to drug delivery, targeting cells and other biomedical applications.

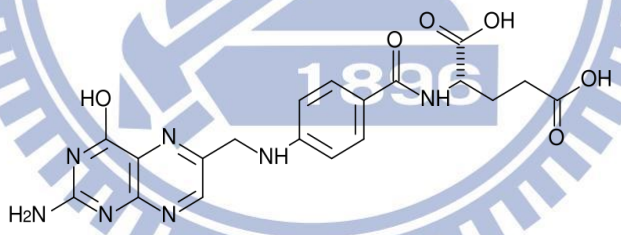

Figure 1.17 Folic acid structure.[38]

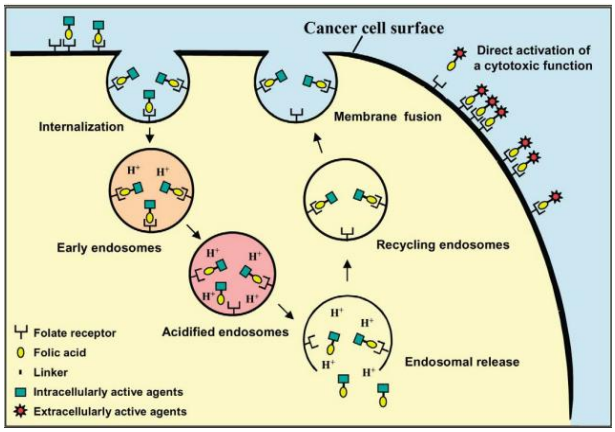

Figure 1.18 Schematic representation of cancer cells by receptor-mediated endocytosis.[39]

1.7 CNT in biomedical application

In the past few years, CNTs have been studies for many interesting biomedical applications. They have been considered for applications in various systems, such as delivery of biological cargos into cells,[13,14,15] biomedical[16] and biosensor devices,[17] bioelectrochemistry[18] and cancer photothermal therapy.[14,19,20] CNTs have strong absorbance in the near-infrared (NIR) region. This unique optical property makes CNTs promising candidates for multifunctional biological transporters and cancer cell killers (Figure 1.19). In our experiment, magnetic carbon nanotube (MCNT) was applied for potential cancer photothermal therapy by NIR laser radiation.

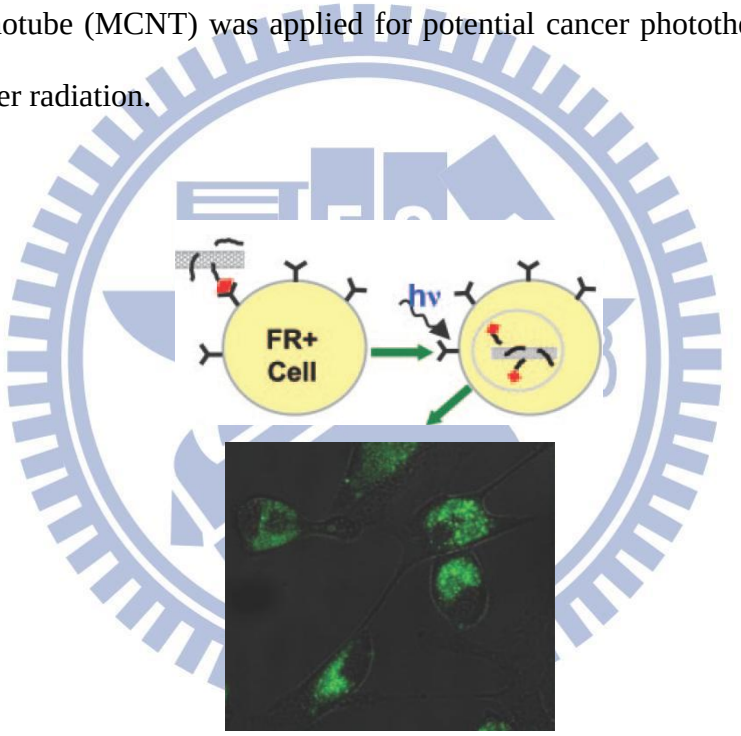

Figure 1.19 Death of cancer cells with rounded cell morphology after NIR laser radiation.[14]

1.8 Cellular uptake of CNT

Cellular uptake of foreign substances may be divided into two types: endocytosis[40] and endocytosis-independent pathways.[41,42] Endocytosis is broadly subdivided into phagocytosis and pinocytosis. Phagocytosis is restricted to specialized cells like macrophages, whereas pinocytosis occurs in all eukaryotic (or mammalian) cell types by at least four basic mechanisms: macropinocytosis, clathrin-mediated

endocytosis (CME), caveolae-mediated endocytosis, and clathrin- and caveolae-independent endocytosis (Figure 1.20). A. Simon-Deckers et al. described that MWCNT uptake may occur via endocytosis. Due to their size (0.1 - 3 μm), MWCNT would rather be internalized in cells through macropinocytosis.[43] N. W. S. Kam et al. prepared Cy3-DNA-SWNT conjugates and observed that nanotube uptake by cells occurs through an energy-dependent endocytosis mechanism.[14] V. Raffaa et al. described that incubation with cells in the presence of endocytosis inhibitor does not influence the cell penetration ability of CNT.[41] K. Kostarelos et al. also observed that cellular internalization of functionalized carbon nanotubes (f-CNTs) does not solely depend on endocytosis. In addition, cellular uptake of f-CNTs is independent of functional group and cell type.[42] However, cellular uptake mechanism is not a clear in literature yet. These apparently contradiction experimental data could be ascribed to the difference in chemical and/or physical properties of CNT.

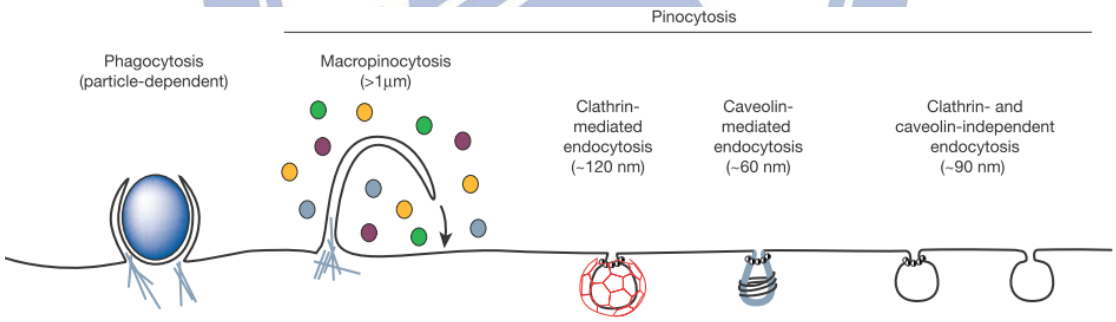

Figure 1.20 Different endocytic pathways.[40]

1.9 Photothermal therapy

Recently, photothermal therapy for selective treatment of tumor cells have been widely investigated because of it is a noninvasive, harmless, and highly efficient therapeutic technique.[14,44,45] This type of therapy is based on nanomaterials extraordinary photon to thermal energy conversion efficiency. With a high absorption cross section of NIR light, this would cause cell death by heat. NIR radiation can

penetrate skin without causing damage to normal tissues due to its weak absorption by tissues. Thus, it can be used to treat specific cells targeted by nanomaterials. Several nanomaterials have strongly absorbed NIR radiation, including gold nanorods, gold nanoshells and SWNTs. Those were recently demonstrated to have potential therapeutic applications (Figeur 1.21).[44,45]

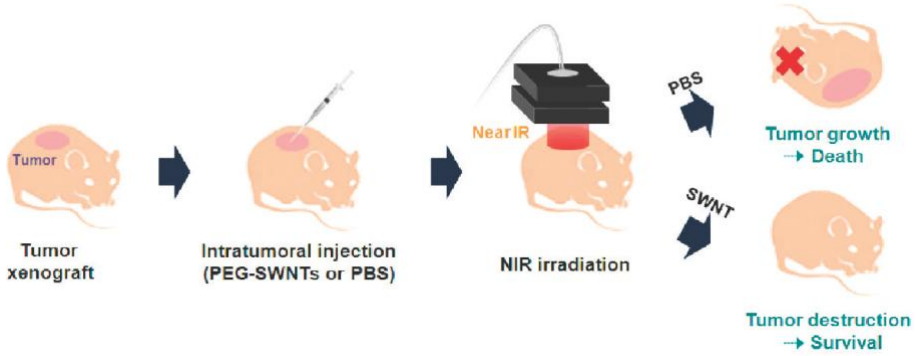

Figure 1.21 Photothermal treatment fot in vivo tumor ablation using PEG-SWNT.[20]

1.10 Motivation of this thesis

Due to current treatments of cancer are still invasive therapies, such as surgery and drug therapy. They still have disadvantages and side effects. The photothermal therapy is a non-invasive way and does not harm normal cells to achieve therapeutic effect. N. W. S. Kam et al. used SWNTs modified DNA and used 808nm laser to kill cancer cells successfully. In addition, in order to speed up the clinic on the accuracy and save time, we need a reagent which can enhance contrast between normal tissue and diseased tissue in MRI. Iron oxide (Fe_3O_4) can be applied as an enhanced contrast reagent. We wish to enclose Fe_3O_4 nanoparticles in CNTs to synthesize MCNTs for the purpose mentioned above. In addition, MCNTs may have the ability to absorb NIR light to kill cancer cells and to monitor tumor lesions. We expect MCNTs can be developed into a multi-functional nanomaterial for biomedical applications.

Chapter 2 Experimental

2.1 Materials

Material	Chemical Formula	Purity	Vendor
Anodic aluminum oxide	Al_2O_3		Whatman Anodisc 13 (pore diameter: 200 nm, length: 60 μm)
Acetylene	C_2H_2	99.9 %	San Fu Chemical Co., Ltd.
Argon gas	Ar	99.9 %	San Fu Chemical Co., Ltd.
Iron (II) chloride tetrahydrate	$FeCl_2 \cdot 4(H_2O)$	＞98 %	Fluka
Iron (III) chloride hexahydrate	$FeCl_3 \cdot 6(H_2O)$	99 %	Riedel-de Haën
Ammonia solution	NH_4OH	28 %	Showa
Tetramethylammonium hydroxide	$C_{14}H_{13}NO$	25 %	Fluka
Sodium hydroxide	NaOH	99 %	Riedel-de Haën
Absolute Ethanol	C_2H_5OH		Sigma-Aldrich
Magnet	NeFeB		Tesla Technology Co., Ltd.
Macrophage			Y.-C. Chen's Lab., Hsinchu , Taiwan
A549 cell			Y.-C. Chen's Lab.

HeLa cell			T.K. Wu Lab., Hsinchu , Taiwan
RPMI 1640 medium with folic acid			Sigma-Aldrich
RPMI 1640 medium without folic acid			Invitrogen
DMEM medium with folic acid			Sigma-Aldrich
DMEM medium without folic acid			Sigma-Aldrich
Phosphate buffered saline			
(3-(4,5-Dimethylthiazol-2-yl)-2,5-diphenyltetrazolium bromide, a tetrazole), MTT	$C_{18}H_{16}BrN_5S$		Sigma-Aldrich
Dimethyl sulfoxide, DMSO	C_2H_6OS	99.9 %	J.T. Baker
Sodium azide	NaN_3	99.5 %	Sigma-Aldrich

2.2 Instrument

Field Emission Scanning Electron Microscope (FESEM)

Hitachi S-4000:

Accelerating voltage: 0.5 ~ 30 kV, Resolution: 1.5 nm at 25 keV

Transmission Electron Microscope (TEM)

JEOL JEM-100CX:

Acceleration Voltage: 20 - 100 kV, Resolution: 0.4 nm

High Resolution Confocal Raman Microscope

HOROBA, Lab RAM HR:

Laser: HeNe: 632.8 nm Wavelength

DPSS: 488 nm, 532 nm Wavelength

Superconducting Quantum Interference Device (SQUID)

MPMS-XL:

Field Range: ± 7.0 Tesla

Temperature range at the sample space: 1.8 K ~ 350 K

UV-Visible Spectrophotometer

Varian Cary 50

Microscope

Nikon ECLIPSE 80i

Hamlet

808 nm Laser

VD-IIA DPSS LASER DRIVER

CLASS IIIB LASER PRODUCTS, LASER MAX POWER < 1 W

2.3 Preparation of MCNTs composites

2.3.1 Template assisted synthesis of CNTs

Several of pieces of AAO templates were placed on a quartz boat and put into a tube furnace. The temperature was raised by a rate of 20 ^{o}C/min under 1 atm of Ar (flow rate: 10 sccm). When the temperature reached 550 or 650 ^{o}C, the carrier gas was closed and the reaction gas acetylene (C_2H_2) was passed into the quartz tube at a rate of 2.8 sccm. The acetylene gas was decomposed at 550 or 650 ^{o}C, while the deposition of carbon into the AAO template occurred. After 30 min, the color of AAO template turned black. The product CNTs inside the AAO channels were obtained.

2.3.2 Fe_3O_4 solution preparation

For Fe_3O_4 solution preparation, iron (III) chloride hexahydrate ($FeCl_3 \cdot 6 (H_2O)$, 99 %) (1 M) and iron (II) chloride tetrahydrate ($FeCl_2 \cdot 4 (H_2O)$, > 98 %) (2 M) were prepared by dissolving the iron salts in an HCl solution (2 M), respectively.

2.3.3 Synthesis of MCNTs

Several CNT@AAO membranes were placed into a three-necked bottle (reaction process shown in Figure 2.1) and pumped below 10^{-2} torr for 5 min. $FeCl_{3(aq)}$ (1 M, 4 mL) and $FeCl_{2(aq)}$ (2 M, 1 mL) solutions were added into the bottle under vacuum atmosphere. The three-necked bottle was slowly shaken for at least 5 min to allow the mixture solution to flow into the CNT@AAO membranes. The pump was closed and Ar gas passed into the three-necked bottle to prevent the Fe_3O_4 nanoparticles from further oxidation. Then, the remaining solution was removed after the mixing. A permanent magnet was placed under the three-necked bottle bottom. The addition of $NH_4OH_{(aq)}$ (4 M, 8 mL) lead to a black precipitate inside and on the CNT@AAO membranes. The solution color changed from brown to black. Then, a drop of tetramethylammonium hydroxide was added to the three-necked bottle to

produce a well dispersed Fe_3O_4 colloidal solution.[25] After the three-necked bottle was slowly shaken, the remaining solution was removed. Deionized water was added to wash the CNT@AAO membranes. This procedure was repeated several times to remove excess ions and tetramethylammonium salt in the suspension. Finally, the washed CNT@AAO membranes were immersed in $NaOH_{(aq)}$ (5 M, 10 mL) at room temperature for three days to remove the AAO membrane. The MCNT was isolated by applying a permanent magnet and was washed several times to neutrality. The resulting product was dried in vacuum to offer MCNTs for further investigation.

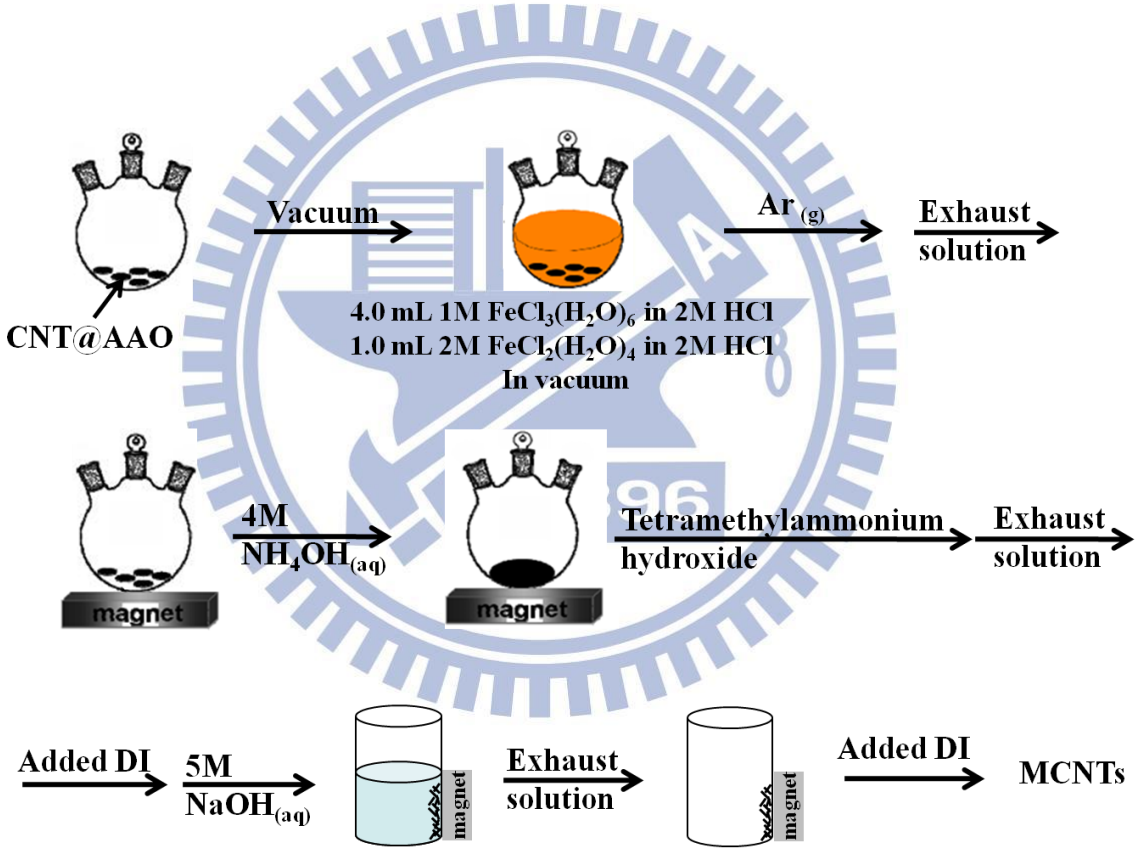

Figure 2.1 MCNTs synthesis procedure.

2.4 *Ex vitro* measurement of heating of a MCNT solution by NIR radiation

MCNT solutions were prepared by sequential dilution in PBS buffer so that the final nanotube concentrations of 2, 1, 0.5 and 0.1 μg/μL were obtained. They were irradiated using a 400 mW laser diode with a wavelength of 808 nm at a power density of 2.04 Wcm^{-2}, a spot size of 0.5 cm diameter and the distance of laser head is about 2 cm from the bottom of well. Temperatures were measured in 30-s intervals with a thermocouple placed inside the solution for a total of 7 min. The thermocouple was placed away from the path of the laser beam to avoid direct exposure to the laser light.

2.5 Cell culture

A549 cells (a human lung carcinoma cell line) were cultured in two different media respectively: the FA-free RPMI 1640 medium and the complete RPMI 1640 medium. They were supplemented with 10 % fetal bovine serum (FBS) and 1 % penicillin-streptomycin in 5 % CO_2 and 95 % air at 37 ^oC in a humidified incubator.

HeLa cells (a human epithelial carcinoma cell line) were cultured in two different media respectively: the FA-free DMEM medium and the complete DMEM medium. They were also supplemented with 10 % fetal bovine serum (FBS) and 1 % penicillin-streptomycin in 5 % CO_2 and 95 % air at 37 ^oC in a humidified incubator.

Macrophages were cultured in complete DMEM medium supplemented with 10 % FBS and 1 % penicillin-streptomycin in 5 % CO_2 and 95 % air at 37 ^oC in a humidified incubator too.

2.6 FR+ Cells and FR- Cells

A549 and HeLa cells were cultured in FA-free RPMI-1640 medium and FA-free DMEM medium, respectively. It is known that FA-starved cells would

overexpress FRs on cell surfaces. A549 and HeLa cells were passaged for at least four rounds in the FA-free medium before use to ensure overexpression of FR on the surface of the cells (FR+ cells). A549 and HeLa cells were prepared by culturing them in abundant FA medium to obtain FR- cells [14].

2.7 Uptake of MCNTs by cells

Firstly, the A549 and HeLa cells were cultured in two different media respectively: the FA-free medium and the complete medium supplemented with 10 % FBS and 1 % penicillin-streptomycin, followed by exposure to MCNT (1 μg/μL, 30 μL) in PBS buffer at 37 ^{o}C for 16 h. Finally, the incubated cells were washed with a PBS buffer (1 mL).

2.8 Laser radiation

A549 cells grown in a 96-well microplate were incubated without MCNTs for 40 h and rinsed with PBS (1 mL). Then, a MCNTs solution (2 μg/μL, 60 μL) was added and exposed to light (808 nm laser) immediately at 2 W/cm^2 for 3 - 7 min. After the laser irradiation, the cells were rinsed with PBS buffer two times and then cell viability was assessed.

2.9 Optical microscopy

The cells were imaged by a Eclipse 80i Nikon microscope. Before the analysis, the cells were seeded in chambered coverslides or 96-well microplate for 24h and then incubated with MCNTs for 16 h. For staining cells, hematoxylin and eosin (H & E) was added to each well and rinsed with PBS (1 mL) at room temperature before imaging.

2.10 Determination of cell cytotoxicity

The cell culture, laser radiation and cell cytotoxicity procedures were shown in Figure 2.3. Cell cytotoxicity assay was used to monitor cell viability with a

colorimetric tetrazolium salt-based assay. To determine the cytotoxicity of MCNTs, cancer cells were cultured in a 96-well microplate for one day and then incubated with different concentrations of MCNTs (A549: 1 to 3 μg/μL, HeLa : 0.5 to 2.5 μg/μL) for 16 h. After rinsed with PBS buffer (1 mL), a microculture tetrazolium (MTT) solution (300 μL) was added to each well to dye the cell. MTT was chemically reduced by cells into formazan. Then, after 4 - 6 h, a dimethylsulfoxide (DMSO) solution (200 μL) was added into each well to dissolve formazan. The formazan concentration and optical absorbance at 560 nm with subtracting a background signal at 630 nm provided a measurement of the metabolically active live cells to determine cell viability. To detect photothermal cell viability, cancer cells were incubated without MCNTs for 48 h and then added an MCNTs solution (2 μg/μL), followed by irradiation (808 nm laser, 2 W/cm^2). Optical density at 560 nm with a subtraction of the signal at 630 nm (O.D 560), was read with a UV-Visible spectrophotometer to determine the viability of the cells.

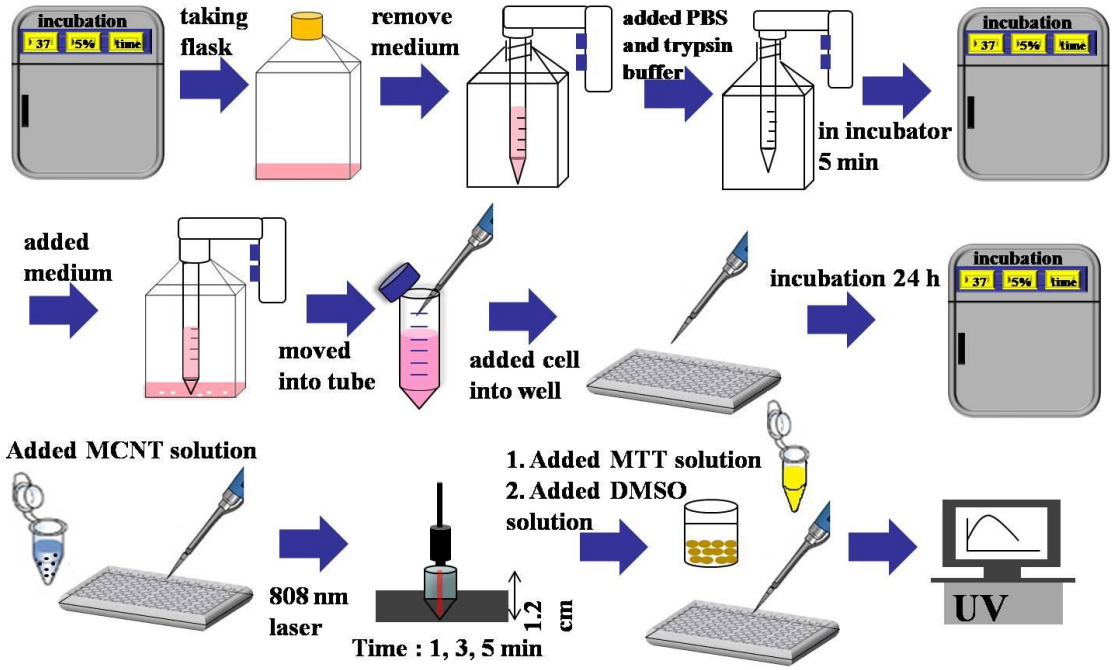

Figure 2.3 Schematic representation of cell culture, laser radiation and cell cytotoxicity procedure.

Chapter 3 Result and Discussion

3.1 Morphology analysis by SEM and TEM

The CNTs were grown inside the channels of AAO membranes at 550, 650 ^{o}C by CVD method. Figure 3.1 (a) and (b) are the top side images while (c) and (d) are the bottom side views, respectively. They clearly show that the surface morphology of the CNT@AAO membrane grown at 550 ^{o}C. Some carbon nanoparticles covering the pores can be found on the top side of the CNT@AAO membrane. The bottom side of the CNT@AAO membrane is not covered so that the pores are exposed. Figure 3.1 (e) and (f) show the cross section of membrane after the AAO was removed by NaOH. The CNTs are not straight tubes. They appear to be collapsed probably because of the wall thickness is too thin. At 650 ^{o}C, the top side of the CNT@AAO membrane is completely covered by carbon (Figure 3.2 (a)). A large number of carbon nanoparticles can be found (Figure 3.2 (b)). Nevertheless, the bottom side of the CNT@AAO membrane is not covered by carbon and the pores are exposed (Figure 3.2 (c) and (d)).

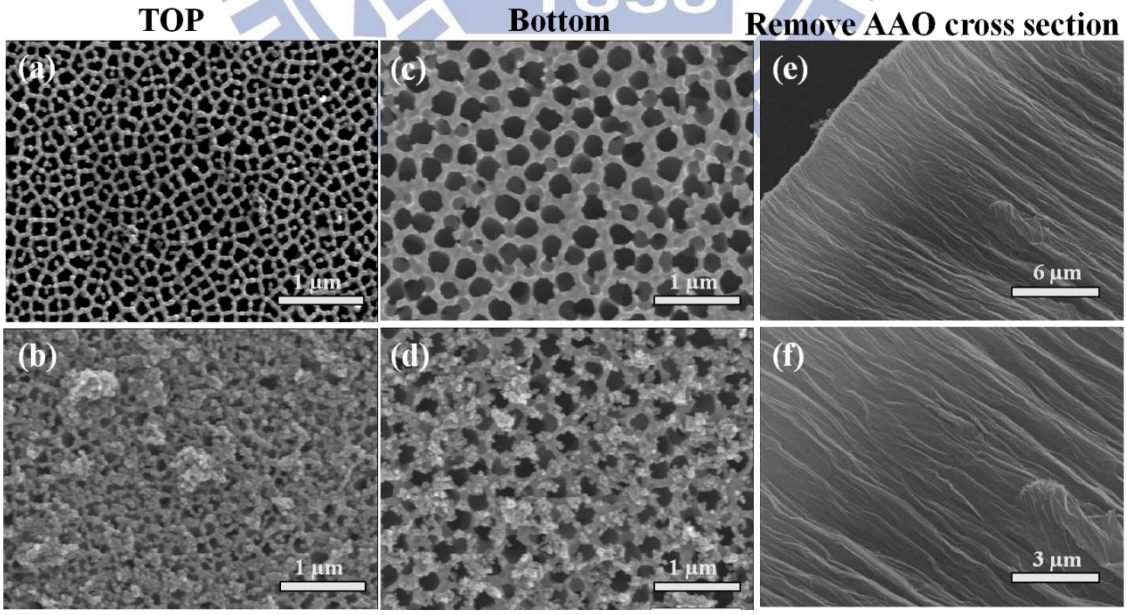

Figure 3.1 SEM images of CNT@AAO grown at 550 ^{o}C. (a) Top view, (b) Another top view, (c) Bottom view, (d) Another bottom view, (e) Cross section of CNT@AAO membrane, (f) is the high magnification image of (e).

Since the top side of the AAO is sealed by carbon, it is not favorable for the ferrofluid to flow into the channels although the CNTs are straight tubes.

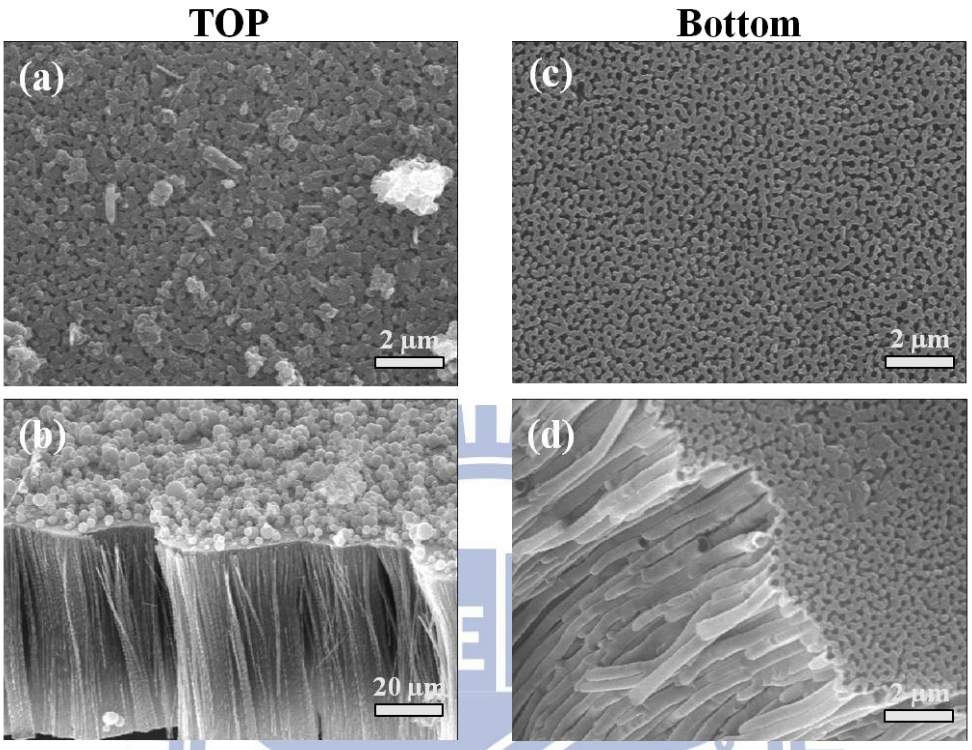

Figure 3.2 SEM images of CNT@AAO grown at 650 ^{o}C. (a) Top view; (c) Bottom view; (b and d) Cross section of CNT@AAO membrane.

MCNTs were synthesized by filling the CNTs grown at 550 ^{o}C with Fe_3O_4 nanoparticles. The overall MCNT synthesis is summarized in Figure 3.3. Firstly, the CNTs are obtained inside the AAO channels by pyrolysis of the acetylene precursor. Then, aqueous solutions containing Fe^{2+} and Fe^{3+} ions are added, following this generates Fe_3O_4 nanoparticles inside the CNT@AAO channels. Finally, the AAO membrane is removed by NaOH to offer the MCNTs.

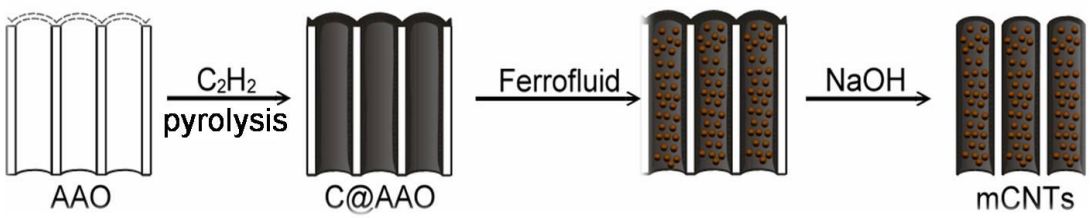

Figure 3.3 MCNTs synthesis mechanism.

Figure 3.4 (a) - (d) shows that the MCNTs are still gathered into bundles after the AAO is removed. This may be due to van der Waal forces among the MCNTs. Furthermore, MCNTs are straight tubes after the iron oxide particles. It is different from the CNT morphology shown in Figure 3.1 (e) at 550 ^{o}C. However, some collapsed morphology can still be found red box in Figure 3.3 (b). Some residual iron oxide particles adsorbed to the MCNTs array can be found in Figure 3.4 (c) and (e). The SEM image and EDS of the CNTs filled with iron oxide particles are shown in Figure 3.4 (d) and (f).

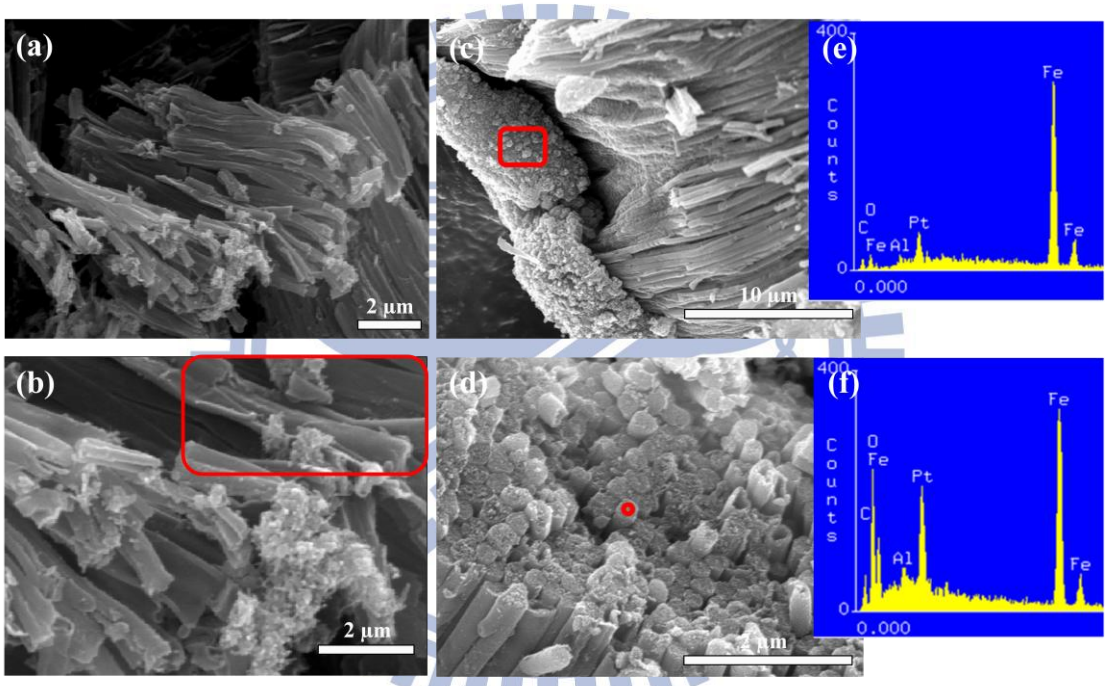

Figure 3.4 (a) and (b) SEM images of MCNT bundles, (c) Side view and (d) top view of the bundles. EDS data (e) from sample in (c), and (f) from sample in (d).

From the TEM images in Figure 3.5 (a) and (c) - (e), it is clear that the MCNT diameter is about 200 – 300 nm, while is similar to the AAO channel diameter. The nanotube wall thickness is about 5 to 10 nm. From types of iron oxide densities are seen inside the CNTs shown in Figure 3.5 (a), (c), (d) and (e). Most of the MCNTs have iron oxide particle densities of Figure 3.5 (a) and (c). Only some CNTs have a small amount of iron oxide particles shown in Figure 3.5 (d) and (e). The SAED

pattern shown in Figure 3.5 (b), displays rings which corresponding to interlayer spacings 0.26, 0.21 and 0.15 nm. They are (311), (400) and (440) planes of Fe_3O_4.

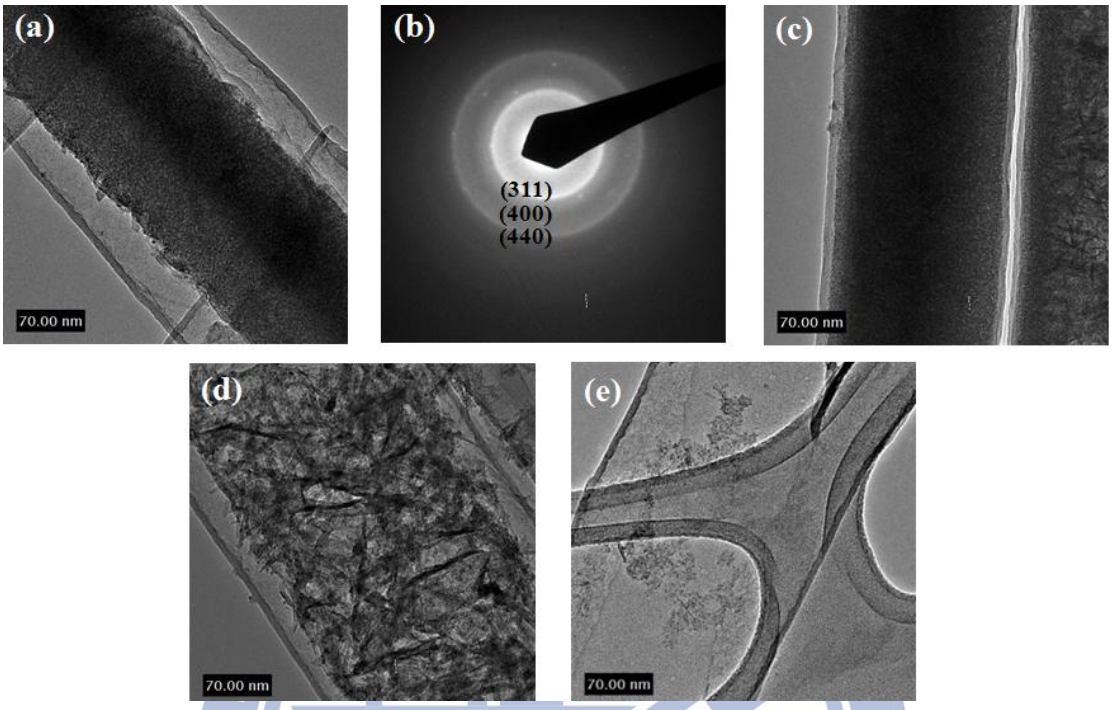

Figure 3.5 TEM images and SAED pattern. (a) and (c) - (e) TEM images, (b) SAED of (a).

3.2 Raman analysis of MCNT

Figure 3.6 shows a Raman spectrum of the MCNT. It clearly shows the Raman active band of the magnetite iron oxide (Fe_3O_4) at 680 cm^{-1},[46] the carbon G-band at 1599 cm^{-1} and the D-band at 1324 cm^{-1}. The values are compare with the results reportedly Z. Sun et al.[47] The MCNT's G-band peak is upshifted about 17 - 19 cm^{-1}. The phenomenon is ascribed to the presence of the Fe_3O_4 nanoparticles inside the CNTs. The carbon peak intensity ratio (I_D/I_G) suggests that the material is non-crystalline.

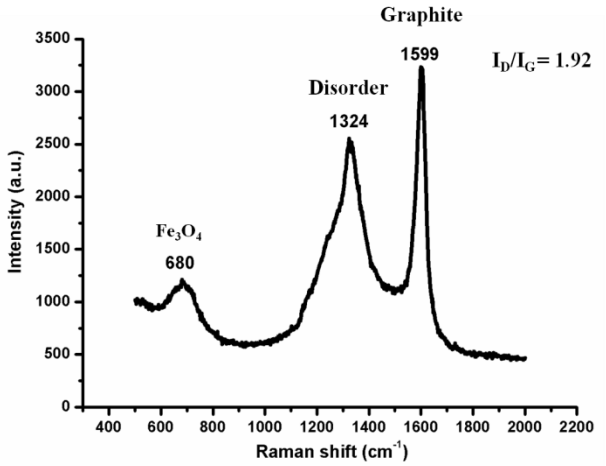

Figure 3.6 Raman spectrum of the MCNT.

3.3 Magnetic properties of MCNT analysized by SQUID

Figure 3.7 shows the magnetization of the MCNTs measured at 5 K and room temperature. The thermal energy is insufficient to induce magnetic moment randomization at 5 K, thus the MCNTs shown typical ferromagnetic hysteresis loop with a remanence of 4.9 emu $g^{-1}$and a coercivity of 702 Oe. However, the thermal energy is high enough to randomize the magnetic moments at 300 K. This leads to a decrease in magnetization, thus the MCNTs show no remanence and coercivity.

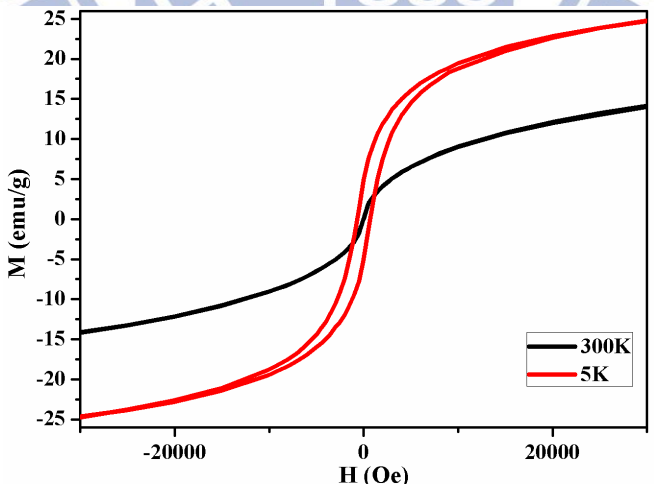

Figure 3.7 Hysteresis loops for MCNTs at 5 K and temperature room.

3.4 Zeta potential of MCNT analysis

The measurement of surface charges of MCNTs can help us to realize their interactions with cells. In addition, it can be a reference value to modify protein

molecules on the MCNT surface in the future. Zeta potentials of the materials are listed in Table 3.1. CNTs in D.I. water (pH 6.18) show a charge value, close to the isoelectric point. Fe_3O_4 nanoparticles show a positive charge value, which is high than that of the CNTs. The charge value of MCNTs is between those of the CNTs and the Fe_3O_4. When CNTs, Fe_3O_4 and MCNTs are placed in PBS buffer solutions (pH 7.4), the values are negative which the charge value of MCNTs is also between those of CNTs and Fe_3O_4.

Table 3.1 Zeta potential values of CNT, Fe_3O_4 and MCNT in D.I water and PBS solution.

	D.I (mV ± SD)	PBS (mV ± SD)
CNT	2.3 ~ -2.3	-12.4 ± 3.7
Fe_3O_4	38.3 ± 1.8	-23.9 ± 0.6
MCNT	29.5 ± 7.8	-17.6 ± 0.3

(mean ± SD, N=3)

3.5 Heating of MCNT solution by NIR radiation

The photothermal effect of MCNT solution was firstly examined *ex vitro* by 808 nm laser irradiation. Figure 3.8 shows that the rate of temperature increase depends on the MCNT concentration. In addition, the temperature of the solution was increased with increasing NIR irradiation time, until a temperature plateau is reached. On the contrary, the temperature does not increase significantly when the NIR irradiates a PBS buffer solution without MCNTs. This verifies that the temperature increase was possibly originated from the MCNTs rather than from the PBS buffer. In addition, it is found that the temperature increase of the Fe_3O_4 solution is lower than the MCNT and the CNT solutions. Therefore, it suggests that the temperature increase of the MCNT solution was mainly contributed by the carbon portion of the composite

materials.

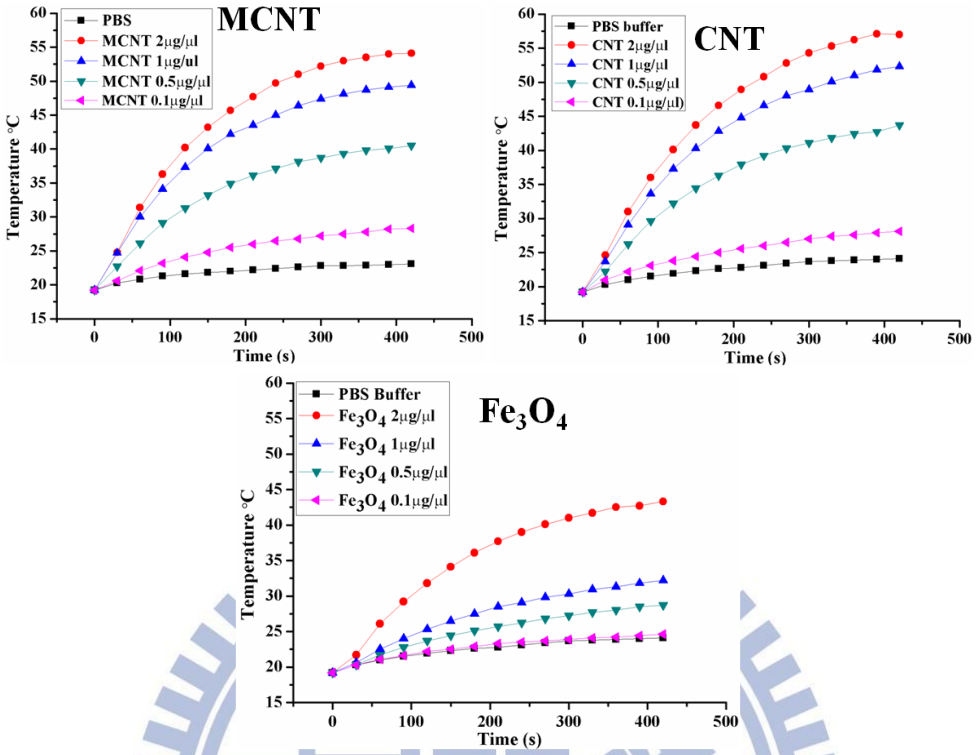

Figure 3.8 *Ex vitro* measurement of heating of contain MCNT, CNT and Fe_3O_4 solutions by NIR radiation.

3.6 Cytotoxicty of MCNT

We investigated the cytotoxic effects of MCNTs using A549 and HeLa cancer cells with the MTT assay technique. A549 and HeLa cells were cultured in complete medium for 16 h with different concentrations of MCNT (A549: 1 μg/μL to 3 μg/μL, HeLa: 0.5 μg/μL to 2.5 μg/μL). We found that the toxicity of the MCNT towards the cells increased with increasing the concentrations. For A549 cells, when the MCNTs concentration increases from 1 to 3 μg/μL, the cell viability decreases from 93 % to 72 % (Figure 3.8). The MCNTs have a good biocompatibility for A549 cells at a concentration below 2 μg/μL (Figure 3.9). For HeLa cells, when the MCNTs concentration increases from 0.5 to 2.5 μg/μL, the cell viability decreases from 79 % to 52 % (Figure 3.10). The high apparent MCNTs toxicity for HeLa cells may be attributed to MCNTs fixed on the formazan crystals, which cannot be dissolved by DMSO, to interfere with the MTT assay.[43,48] In this experiment, A549 and HeLa cells

have difference in MCNTs uptake behavior. Presumably, MCNTs can penetrate membrane into HeLa cells easily, but cannot penetrate A549 cell membrane well.

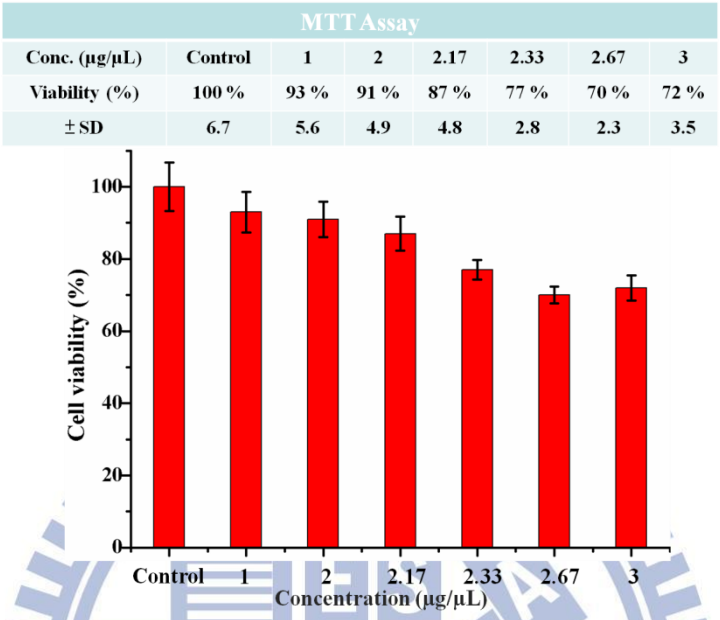

Figure 3.9 Cytotoxicty of MCNTs to A549 cells at different concentrations. The volume of each concentration was 30 μL. Bars (mean ± SD, N = 4).

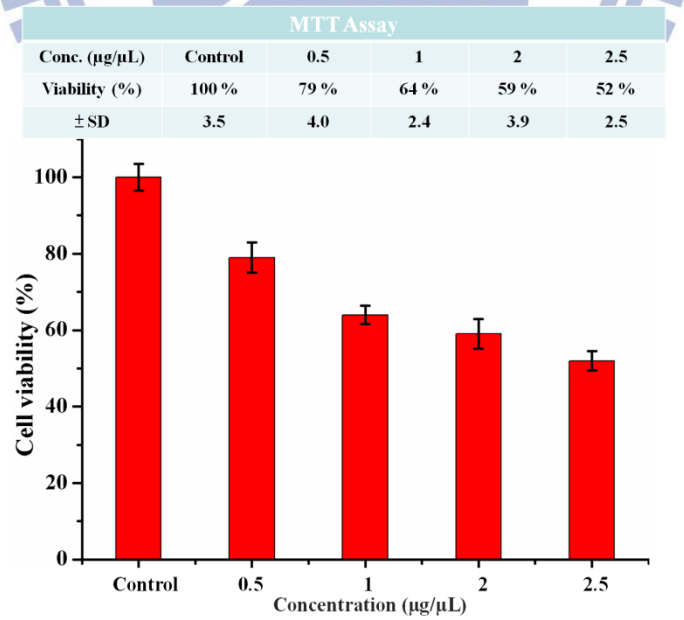

Figure 3.10 Cytotoxicty of MCNTs to HeLa cells at different concentrations. The volume of each concentration was 30 μL. Bars (mean ± SD, N = 4).

3.7 Thermal destruction of cancer cells *in vitro* by MCNTs

We use a 400 mW laser diode with a wavelength of 808 nm at a power density of 2.04 Wcm^{-2} and a spot size of 0.5 cm diameter for 3, 5 and 7 min to irradiate the cancer cells. According to Figure 3.8, the MCNT concentration of 2 μg/μL (60 μg/ 30 μL). It has a great biocompatibility to A549 cells. However, in this experiment, in order to measure *in vitro* temperature we added a PBS buffer solution (30 μL) to the well for a convenient measurement and lead to concentration change into 1 μg/μL (60 μg/ 60 μL). The experimental data prove when the concentration was diluted to 60 μg/ 60 μL, the biocompatibility is still good (Figure 3.11). Therefore, we used 60 μg/ 60 μL as the experimental condition in this experiment. Furthermore, *in vitro* temperature measurement method is different from *ex vitro*. The former measurement method is putting the thermocouple into solution after laser irradiation. We found that the *in vitro* temperature is 37.2 to 40 ^{o}C. The temperature can kill the cancer cells by the NIR laser radiation in our experiment. Although, in our knowledge of killing the cancer cells is about 41 to 43 ^{o}C.[49] We think *in vitro* the localized temperature may be higher than the overall solution temperature because the solution temperature we measured reached a thermal equilibrium. From the experimental result, A549 cells treated with the MCNTs showed extensive cell death after heating with the NIR irradiation, as shown in the data presented in Figures 3.11 and 3.12.

After Laser MTT Assay						
Conc. (μg/μL)	Control	MCNT	Laser 7 min	MCNT+Laser 3 min	MCNT+Laser 5 min	MCNT+Laser 7 min
Viability (%)	100 %	101 %	105 %	30 %	11 %	13 %
± SD	4.4	4.8	6.4	3.5	1.5	1.9

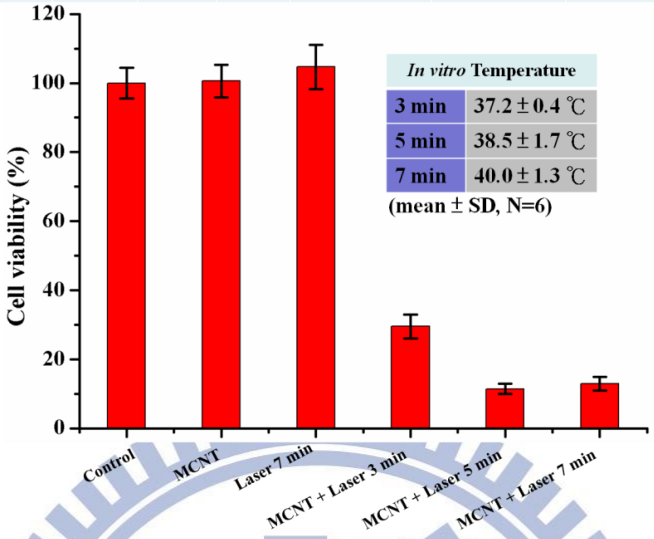

Figure 3.11 Bars (mean ± SD, N = 4).Viability of A549 cancer cells under different treatments. Cells treated with MCNT only, laser only and with MCNT-laser. Cells without treatment were used as the control experimental. The inset table is *in vitro* solution temperature.

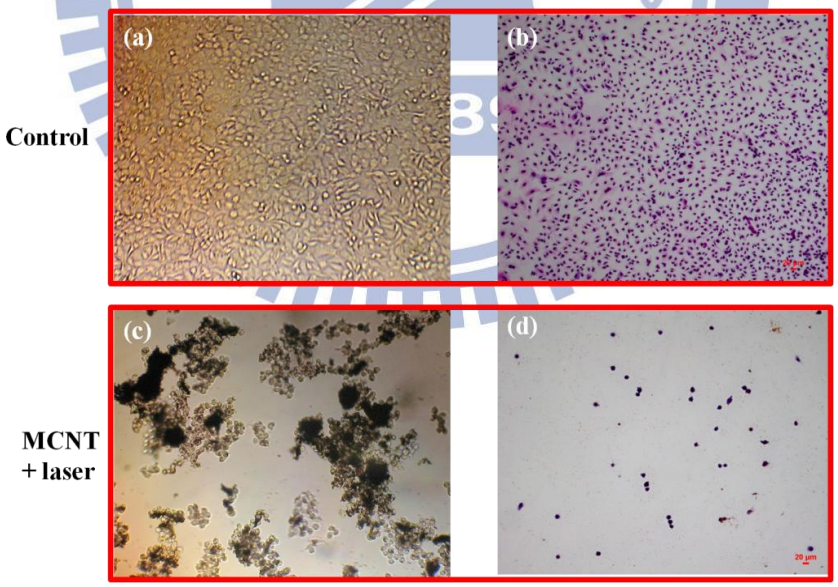

Figure 3.12 Optical images of A549 cancer cells under different treatments. (a) and (b) is without the MCNT treatment are used as the control experiments. (c) and (d) MCNT followed by laser irradiation treatment. H&E staining of A549 cancer cells, (b) control and (d) MCNT followed by laser irradiation treatment. (a) and (c) were imaged by Hamlet optical microscope. (b) and (d) were imaged by Nikon Microscope ECLIPSE 80i.

3.8 Cell uptake of MCNTs with and without FA medium

At first, we used A549 lung cancer cells to test whether they can uptake MCNTs. However, we found that MCNTs are not uptake by A549 cells with or without the FA medium. The MCNTs can only attach to the cell surfaces (Figure 3.13). We suppose that the MCNT lengths affect A549 cells' ability to uptake the MCNTs. Therefore, we specifically chose macrophage cells for more investigations. This is because they are involved in immune defense systems of vertebrate animals by engulfing pathogens and can easily incorporate extraneous particles via phagocytosis.[50] In Figure 3.14, we observe that the MCNTs are uptaken by the macrophage cells. This suggests that the MCNTs lengths are not a problem for the macrophage cells (Figure 3.14). Then, we tried another cancer cell, HeLa cell. After incubation for 2 h, it was found that few MCNTs are uptaken by HeLa cells with or without a FA medium (Figure 3.15 (a) and (d)).

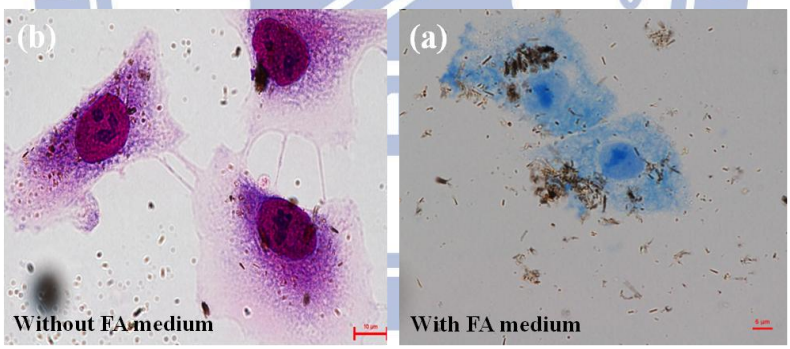

Figure 3.13 A549 cancer cells incubation (a) with FA medium (b) without FA medium for 16 h. The scale bar corresponds to (a) 5 µm, (b) 10 µm.

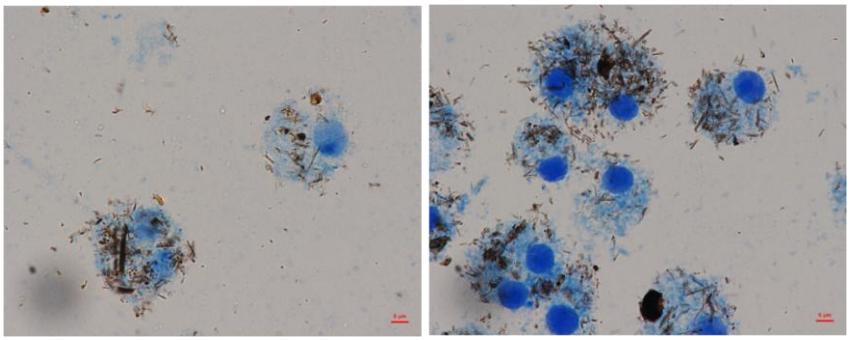

Figure 3.14 Macrophage cells incubation with FA medium for 16 h. Bar 5 µm.

After incubation for 16 h, MCNTs are uptaken by the HeLa cells. They could more across the cell membranes into the cells (Figure 3.15 (b) and (e)). The cellular uptake in cells exposed to MCNT in the FA-free culture medium is much higher than those in the culture medium with FA. We used a trypsin solution to confirm whether the MCNTs can be internalized into the cells. According to Figure 3.16, we show that the MCNTs are indeed internalized in the HeLa cells. However, when CNTs are used, the same phenomenon is not seen (Figure 3.17). We suspect that the surface structures of the CNTs may be different from those of the MCNTs. This may prevent the CNTs from penetrating the cell membranes.

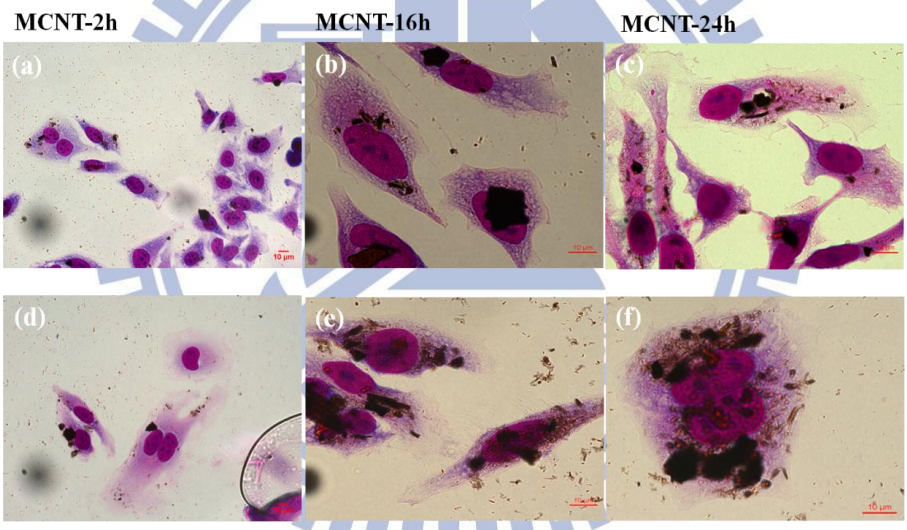

Figure 3.15 Optical microscope images of HeLa cells. (a)-(c) With MCNTs dispersed in a complete medium. (d)-(e) With MCNTs dispersed in an FA-free medium.

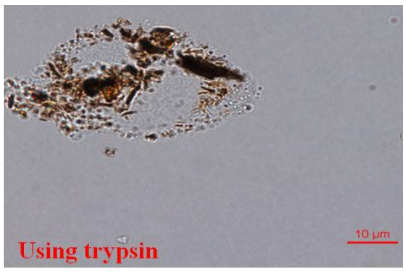

Figure 3.16 Optical microscope image of a HeLa cell after trypsinization.

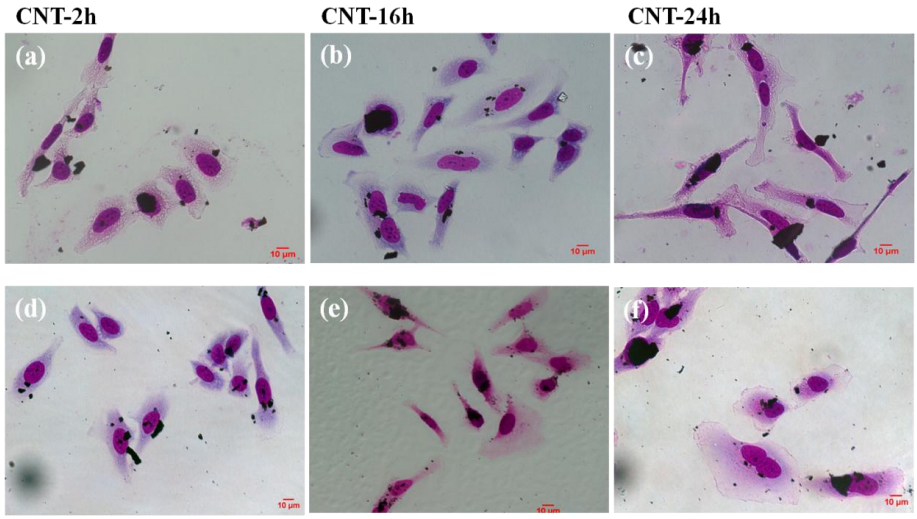

Figure 3.17 Optical microscope images of HeLa cells. (a)-(c) With CNTs dispersed in a complete cell culture medium. (d)-(e) With CNTs dispersed in an FA-free cell culture medium.

Finally, we explored the uptake pathway of MCNTs by cells whether an endocytosis or an endocytosis-independent pathway may be inoperation. We used sodium azide as an endocytosis inhibitor agent,[41,42] at a concentration of 5 mg/mL for 6 h to stop the cell endocytosis. We found that the incubation with the sodium azide pre-trement does not affect MCNTs uptake by the cells (Figure 3.18). It is clear that the uptake mechanism is likely to be an endocytosis-independent pathway.

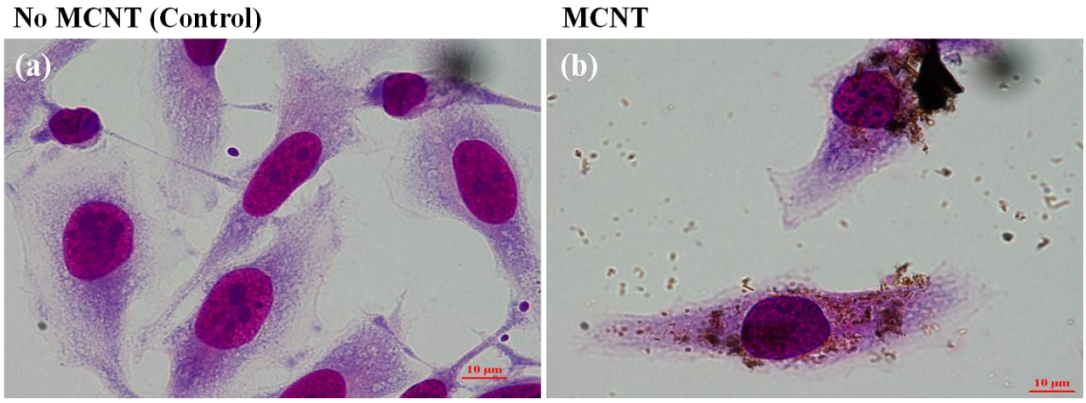

Figure 3.18 HeLa cells pre-treated with sodium azide for 6 h before to perform the assay. HeLa cells incubated with (a) no MCNTs, (b) MCNTs. Scale bar: 10 μm.

Chapter 4 Conclusion

In conclusion, we successfully synthesized MCNTs by a simple process. We also demonstrate that the MCNTs have a great biocompatibility to A549 cancer cell and can absorb NIR radiation to kill the cancer cells *in vitro*. Further studies are needed to investigate the effectiveness of MCNTs conjugated with biomarkers such as folic acid for selective photothermal therapy of cancers.

On the other side, we demonstrated that HeLa cells cultured in FA-free medium took up more MCNTs than HeLa cells cultured in medium with FA after incubation for 16 h. Furthermore, we used sodium azide as an endocytosis inhibitor to explore the uptake of MCNTs by HeLa cells. We observed that cellular internalization of MCNTs was not influenced even under the endocytosis inhibiting condition. It is clear that the uptake mechanism is likely to be an endocytosis-independent pathway.

We also expect that the MCNTs can act as a contrast enhancement agent for magnetic resonance imaging (MRI) signals in future clinical diagnosis.

References

1. C. R. Martin, *Chem. Mater.*, **1996**, *8*, 1739.
2. F. Li, J. B. Wiley, *J. Mater. Chem.*, **2008**, *18*, 3977.
3. L. S. Wang, C. Y. Lee, H. T. Chiu, *Chem. Comm.*, **2003**, 1964.
4. J. M. Moon and A. Wei, *J. Phys. Chem. B*, **2005**, *109*, 23336.
5. J. Li, M. Moskovits, T. L. Haslett, *Chem. Mater.*, **1998**, *10*, 1963.
6. G. Cao, D. Liu, *Adv. Colloid Interface Sci.*, **2008**, *136*, 45.
7. J. D. Klein, R. D. Herrick, D. Palmer, M. J. Sailor, *J. Chem. Mater.*, **1993**, *5*, 902.
8. M. Wilson, K. Kannangar, B. Raguse, G. Smith, M. Simmons, *Nanotechnology: Basic Science and Emerging Technologies*, UNSW Press, **2002**.
9. H. W. Kroto, J. R. Heath, S. C. O'Brien, R. F. Curl, R. E. Smally, *Nature*, **1985**, *318*, 162.
10. W. Krästschmer, L. D. Lamb, K. Fortiropoulos, D. R. Huffman, *Nature*, **1990**, *347*, 354.
11. S. Iijima, *Nature*, **1991**, *354*, 56.
12. A. A. Busnaina, *Nanomanufacturing Handbook*, CRC Press, **2007**.
13. N. W. S. Kam, T. C. Jessop, P. A. Wender, H. Dai, *J. Am. Chem. Soc.*, **2004**, *126*, 8650.
14. N. W. S. Kam, M. O'Connell, J. A. Wisdom, H. Dai, *PNAS*, **2005**, *102*, 11600.
15. X. Yang, Z. Zhang, Z. Liu, Y. Ma, R. Yang, Y. Chen, *J. Nanopart. Res.*, **2008**, *10*, 815.
16. R. H. Baughman and A. A. Zakhidov, *Science*, **1999**, *284*, 1340.
17. R. J. Chen, S. Bangsaruntip, K. A. Drouvalakis, N. W. Kam, M. Shim, Y. Li, W. Kim, P. J. Utz, and H. Dai, *PNAS*, **2003**, *100*, 4984.
18. J. J. Gooding, R. Wibowo, J. Liu, W. Yang, D. Losic, S. Orbons, F. J. Mearns, J. G. Shapter, and D. B. Hibbert, *J. Am. Chem. Soc.*, **2003**, *125*, 9006.
19. F. Zhou, D. Xing, Z. Ou, B. Wu, D. E. Resasco, W. R. Chen, *J. Biomed. Opt.*, **2009**, *14*, 021009.
20. H. K. Moon, S. H. Lee, H. C. Choi, *ACS Nano*, **2009**, *3*, 3707.
21. S.-Y. Wang, K.-C. Ho, S.-L. Kuo, N.-L. Wu, *J. Electrochem. Soc.*, **2006**, *153*, A75.
22. N. A. Frey, S. Peng, K. Cheng, S. Sun, *Chem. Soc. Rev.*, **2009**, *38*, 2532.
23. H. B. Fredj, S. Helali, C. Esseghaier, L. Vonna, L. Vidal, A. Abdelghani, *Talanta*, **2008**, *75*, 740.
24. J. Kim, Y. Piao, T. Hyeon, *Chem. Soc. Rev.*, **2009**, *38*, 372.
25. F.-Y. Cheng, C.-H. Su, Y.-S. Yang, C.-S. Yeh, C.-Y. Tsai, C.-L. Wu, M.-T. Wu,

D.-B. Shieh, *Biomaterials*, **2005**, *26*, 729.
26. G. M. Lanza, P. Winter, S. Caruthers, A. Schmeider, K.Crowder, A. Morawski, H. Zhang, M. J. Scott, S. A. Wickline, *Curr. Pharm. Biotechnol.*, **2004**, *5*, 495.
27. D. E. Speliotis, *J. Magn. Magn. Mater.*, **1999**, *193*, 29.
28. O. Bomatı´-Miguel, M. P. Morales, P. Tartaj, J. Ruiz-Cabello, P. Bonville, M. Santos, X. Zhao, S. Veintemillas-Verdaguer, *Biomaterials*, **2005**, *26*, 5695.
29. C. Gao, W. Li, H. Morimoto, Y. Nagaoka, T. Maekawa, *J. Phys. Chem. B*, **2006**, *110*, 7213.
30. A. Leonhardt, S. Hampel, C. Müller, I. Mönch, R. Koseva, M. Ritschel, D. Elefant, K. Biederman, B. Büchner, *Chem. Vap. Deposition*, **2006**, *12*, 380.
31. S. Hampel, A. Leonhardt, D. Selbmann, K. Biederman, D. Elefant, C. Müller, T. Gemming, B. Büchner, *Carbon*, **2006**, *44*, 2316.
32. J. Zhang, J. Du, D. Ma, G. Xi, X. Hu, Y. Qian, *Solid State Commun.*, **2007**, *144*, 168.
33. X. H. Wang, H. Orikasa, N. Inokuma, Q. H. Yang, P. X. Hou, H. Oshima, K. Itoh, T. Kyotani, *J. Mater. Chem.*, **2007**, *17*, 986.
34. G. Korneva, H. Ye, Y. Gogotsi, D. Halverson, G. Friedman, J. C. Bradley, K. G. Kornev, *Nano Lett.*, **2005**, *5*, 879.
35. William D. Callister, Jr., *Materials Science and Engineering an Introduction Sixth Edition*, U.S.A Wiley., **2003**.
36. http://en.wikipedia.org/wiki/Ferromagnetism, from Wikipedia, the Free Encyclopedia, Ferromagnetism, Retrieved Mar. 27, 2010.
37. G. L. Hornyak, J. J. Moore, H. F. Tibbals, J. Dutta, *Fundamentals of Nanotechnology*, CRC Press, **2009**.
38. S. L. Kim, H. J. Jeong, E. M. Kim, C. M. Lee, T. H. Kwon, M. H. Sohn, *J. Korean Med. Sci.*, **2007**, *22*, 405.
39. Y. Lu, P. S. Low, *Adv. Drug Deliv. Rev.*, **2002**, *54*, 675.
40. S. D. Conner, S. L. Schmid, *Nature*, **2003**, *422*, 37.
41. V. Raffaa, G. Ciofania, S. Nitodasb, T. Karachaliosb, D. D'Alessandrod, M. Masinie, A. Cuschieria, *Carbon*, **2008**, *46*, 1600.
42. K. Kostarelos, L. Lacerda, G. Pastorin, W. Wu, S. Wieckowsli, J. Luangsivilay, S. Godefroy, D. Pantarotto, J.-P. Briand, S. Muller, M. Prato, A. Bianco, *Nature Nanotechnology*, **2007**, *2*, 108.
43. A. S. Deckers, B. Gouget, M. M. L'Hermite, N. H. Boime, C. Reynaud, M. Carrière, *Toxicology*, **2008**, *253*, 137.
44. J. Kim, Y. Piao, T. Hyeon, *Chem. Soc. Rev.*, **2009**, *38*, 372.
45. P. K. Jain, I. H. El-Sayed, and M. A. El-Sayed, *Nanotoday*, **2007**, *2*, 18.
46. J.-Y. Lee, B.-C. Kang, D.-Y. Jung, J.-H. Booa, *J. Vac. Sci. Technol. B*, **2007**, *25*,

1516.
47. Z. Sun, Z. Liu, Y. Wang, B. Han, J. Du, J. Zhang, *J. Mater. Chem.*, **2005**, *15*, 4497.
48. X. Zhang, X. Wang, Q. Lu, C. Fu, *Carbon*, **2008**, *46*, 453.
49. 李偉銘，葉晨聖，國立成功大學化學研究所碩士論文，2008, 27 頁。
50. J. H. Choi, F. T. Nguyen, P. W. Barone, D. A. Heller, A. E. Moll, D. Patel, S. A. Boppart, M. S. Strano, *Nano Lett.*, **2007**, *7*, 861.